

The Influence of Surface Plasmons on Excited State Dynamics in PTCDA

by

N. A. Azarova

B.S., Wake Forest University, 2010

A thesis submitted to the

Faculty of the Graduate School of the

University of Colorado in partial fulfillment

of the requirements for the degree of

Master of Science

Department of Electrical, Computer, and Energy Engineering

2012

This thesis entitled:
The Influence of Surface Plasmons on Excited State Dynamics in PTCDA
written by N. A. Azarova
has been approved for the Department of Electrical, Computer, and Energy Engineering

Dr. Won Park

Dr. Justin Johnson

Dr. Garret Model

Date_____

The final copy of this thesis has been examined by the signatories, and we find that both the content and the form meet acceptable presentation standards of scholarly work in the above mentioned discipline.

Azarova, N. A. (M.S., Electrical Engineering)

The Influence of Surface Plasmons on Excited State Dynamics in PTCDA

Thesis directed by Dr. Won Park

Organic thin film solar cells can be paired with nanostructured substrates to overcome the issue of narrow spectral absorption in a thin-film configuration. The nanostructured surface acts not only as an effective scattering back reflector to increase the light path within the absorbing thin film but also affords plasmonic activity. The interface between the metal and the absorbing chromophore supports surface plasmon modes. The associated strong electromagnetic field can potentially couple with excitations of the chromophore, altering its exciton dynamics. Such a plasmon-exciton coupling can lead to control over excitation processes, namely singlet fission. Singlet fission is a sharing of excited state energy between chromophores that may regulate instances of multi-exciton generation, allowing the solar cell efficiency to exceed the thermodynamical Shockley-Queisser limit.

The current investigation focuses on hybridization of the plasmon and molecular exciton. We coat an organic semiconductor, 3,4,9,10-perylenetetracarboxylic dianhydride (PTCDA), on the nanogratings consisting of lines of Ag on a substrate coated with a thick Ag backing. A dielectric spacer layer is included between the organic and the metal in some samples to eliminate any reaction between the two. The SP resonance of the grating is tuned through a PTCDA exciton line by sweeping the incident wave vector. Successful anticrossing between the plasmon and the exciton peaks would be observed in steady-state reflectance data as a function of angle. Though a detailed analysis of reflectance spectra has not been completed, the potential for plasmon-exciton hybridization is demonstrated.

Dedication

Dedicated to all who will be working in the field of organic photovoltaics, photovoltaics in general and renewable energy research as a whole in the future.

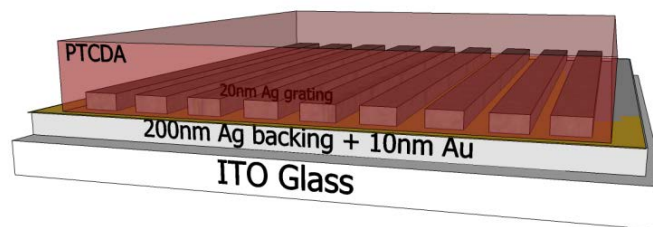


Figure 1: An organic plasmonic solar cell (donor layer and top contact not shown).

Acknowledgements

I am grateful to my class and lab mates who were great friends throughout graduate school, those who helped with fabrication, SEM imaging and did simulations. I especially thank both my CU and NREL advisers for guiding me along the scientific and intellectual endeavor that is this thesis and the grant from the LDRD program at NREL which made this work possible.

Спасибо!

Contents

Chapter

1	Introduction	1
1.1	Theoretical Background	3
1.1.1	EM Waves and Matter	3
1.1.2	Dispersion of Light in Metals	5
1.1.3	Surface Plasmon Dispersion	9
1.1.4	Grating Coupling to Surface Plasmons	13
1.1.5	Splitting of the Grating Resonance Line	14
1.2	Singlet Fission	15
1.3	PTCDA	17
2	Fabrication of Nanogratings	21
2.1	Laser Interference Lithography	21
2.2	Nanoimprint Lithography	27
2.3	Evaluation of Gratings	29
3	Assessment of Surface Plasmon Effect	39
3.1	Angle-Resolved, Variable Polarization Transmission/Reflection Setup	39
3.2	Fitting Procedure	41
3.3	Fits	46
3.3.1	Bare PTCDA	46
3.3.2	Bare Grating	47

3.3.3	Grating with Oxide	50
3.3.4	Grating with Oxide and PTCDA	52
3.4	Conclusions	55
4	Future Directions for Plasmon-Exciton Coupling in PTCDA	56
	Bibliography	57

Tables

Table

2.1	Grating parameters of the first type	29
2.2	Grating parameters of the second type	35
3.1	Freely adjustable parameters in the chi-squared global fit	45

Figures

Figure

1	An organic plasmonic solar cell	iv
1.1	Reflectivity of silver	7
1.2	The real part of the dielectric function of silver	8
1.3	Dispersion relation of the bulk plasmon	8
1.4	Cartoon of surface plasmons and their associated EM field	10
1.5	Dispersion of surface plasmon polaritons	12
1.6	Surface plasmon polariton dispersion for coupling by a grating	14
1.7	Jablonski diagram of singlet fission	16
1.8	Chemical and bulk crystal structure of PTCDA	17
1.9	Linear absorption of PTCDA films of varying thickness	19
1.10	Individual R spectra of a 10nm PTCDA film and a bare grating.....	20
2.1	Schematic of the laser interference lithography setup	22
2.2	Two-beam interference holography	22
2.3	Correct arrangement of LIL setup for desired pitch	23
2.4	Lloyd's mirror interferometer	26
2.5	Steps of nanoimprint lithography	27
2.6	SEM images of the first set of the 2D nanohole array	31
2.7	SEM images of first set of 2D nanohole array post rigorous lift-off	33
2.8	SEM images of second set of 2D nanohole array gratings	34

2.9	SEM images of the Ag line 1D grating	36
2.10	SEM images of successful gratings	38
2.11	A Sample transmittance spectra of a successful grating	38
3.1	Simulation of plasmon-exciton anticrossing	40
3.2	Angle-resolved, variable polarization reflection/transmission setup	41
3.3	R spectra of 10nm PTCDA on a thick Ag backing	46
3.4	Fit to a R spectra of 10nm PTCDA on a thick Ag backing	47
3.5	R spectra of a bare grating: splitting vs. incident angle	48
3.6	Fit to R spectra of bare grating	49
3.7	R spectra of a grating with a thin and thick oxide layer	51
3.8	Fit to R spectra of a grating with thin oxide layer	52
3.9	R spectra of PTCDA on grating, with and without dielectric spacer layer	53

Chapter 1

Introduction

PV technologies have been acknowledged as an elegant clean energy alternative but have historically been shrouded in a political interpretation deeming them far too expensive and rendering their somewhat thwarted commercialization. While this characterization had merit during the industry's infancy, costs of both PV modules and installation and maintenance have recently fallen dramatically. Manufacturers were able to drop prices of modules by 50% from \$4.00/W in 2008 to \$2.00/W in 2009 due to advances in manufacturing processes as well as improvements in cell efficiencies. Improved performance of balance-of-system components, things like batteries, mounting structures and inverters, have seen a steady decrease in installation and maintenance costs since 2004. Financing costs have likewise decreased due to decision-makers' greater comfort with providing policy support through, for example, feed-in tariffs. Falling costs have accordingly resulted in a boost in deployment of PV systems, which increased by over 50% in 2010 to 28.7GW in 2011 [53]. Deployment has occurred even at the level of consumer electronics, with companies such as Brunton and Goal Zero selling portable PV panels directly to consumers. Both companies sell foldable and flexible solar panels geared towards camping enthusiasts. Brunton reports using both CIGS and polycrystalline and amorphous silicon semiconductors. Products of both companies have few but very good reviews on the online outdoor retailer backcountry.com.

Efforts to decrease the cost of PV technologies can happen at the deployment as well as fabrication level. At the latter, organic thin-film PV have made headway with record cell efficiencies over 8% [54]. Organic thin films maintain cost efficiency by reducing the amount of

absorbing material needed as well as affording room temperature, solution processable fabrication [55]. However, they inherently suffer from low absorbance of near-bandgap light. Organic photovoltaic absorbers must be optically thick to achieve full absorption of the solar spectrum but physically thin enough for better exciton dissociation and, subsequently, improved carrier extraction. A design approach utilizing metallic nanostructures that support surface plasmons (SPs) has been shown to significantly increase light trapping in thin-film solar cells. The nanostructured surface lengthens the optical path of light in the organic semiconductor (OS) due to increased scattering off the nanofeatures, leading to enhanced absorption in the thin organic absorber layer [56]. Proper engineering of these plasmonic structures will not only enhance absorption but may also result in coupling between the SPs and excited states of the organic chromophore. This could enable a control of the excited state dynamics of the organic absorber, specifically nonradiative processes leading to the occurrence of singlet fission (SF). SF is a third-generation photoconversion scheme that can potentially increase the efficiency of current organic solar cells through carrier multiplication.

This thesis presents the preliminary efforts to progress the field of utilizing third generation photophysics for enhanced solar energy conversion by investigating coupling of excitations of the OS PTCDA, a small-molecule perylene derivative, to SPs supported by a nanograting substrate. SF has been confirmed in several polyacenes, but no work has been reported on harnessing SF in PTCDA by electronic coupling. In the following sections, I start with a theoretical background of the grating behavior, explaining the SP dispersion relation and its consequences on plasmon/PTCDA coupling. I also give a brief description of singlet fission as the relevant mechanism for carrier multiplication as well as a description of the optical properties of PTCDA. In Chapter 2, I present the lithographic technique by which I fabricated

gratings for use in the plasmon/chromophore system along with a visual guide of the progress of fabrication. Chapter 3 will introduce steady-state properties of PTCDA on the nanogratings and chapter 4 has perspectives and hopes for future research.

1.1 Theoretical Background

This chapter provides a theoretical treatment of surface plasmons (SPs) within the classical framework of Maxwell's equations and the plasma model of the optical properties of metals. First, the formula for the relative permittivity of metals and light dispersion in the bulk of a metal are derived. SPs are introduced as a special case of solutions to Maxwell's equations corresponding to confined waves. The results are compared to the behavior of a real metal. Finally, grating coupling of light to SPs is discussed. The chapter concludes with a brief discussion about the consequences of grating coupling to the research presented in this thesis.

1.1.1 Electromagnetic Waves and Matter

Electronic properties of metals can be explained with an analogy of plasma over a wide frequency range. In the plasma, or Drude, model, a gas of free electrons of number density n , typically on the order of 10^{23}cm^{-3} , moves against a fixed background of positive ions [3]. The plasma model disregards electron-electron interactions and the lattice potential, and instead absorbs aspects of the band structure into the effective mass of each electron [2]. Even with these simplifications, the plasma model can successfully explain some experimental phenomena. The plasma frequency, for example, is the reason most metals are highly reflective for frequencies in the visible spectral range, but start to allow the propagation of electromagnetic (EM) waves at higher frequencies.

Maxwell's equations provide the fundamental governing classical framework of electromagnetism. The SP corresponds to solutions of Maxwell's equations, shown below without source terms and for propagation through macroscopic media.

$$\begin{aligned}
 \nabla \cdot \mathbf{D} &= 0 \\
 \nabla \cdot \mathbf{B} &= 0 \\
 \nabla \times \mathbf{E} &= -\frac{\partial \mathbf{B}}{\partial t} \\
 \nabla \times \mathbf{H} &= \frac{\partial \mathbf{D}}{\partial t}
 \end{aligned} \tag{1.1}$$

with dielectric displacement \mathbf{D} , electric field \mathbf{E} , magnetic field \mathbf{H} and magnetic induction \mathbf{B} . Information about the medium comes from the relations below, further linking the four macroscopic electric and magnetic fields

$$\mathbf{D} = \varepsilon_0 \varepsilon \mathbf{E} \tag{1.2}$$

$$\mathbf{B} = \mu_0 \mu \mathbf{H} \tag{1.3}$$

ε_0 and μ_0 are the electric permittivity and magnetic permeability of free space, respectively. This description considers only isotropic and homogenous media, making $\mu(\omega)$ and $\varepsilon(\omega)$ scalar quantities, and having a linear polarization and magnetization response to the external fields. Furthermore, this discussion is limited to electric polarization effects, so only nonmagnetic ($\mu(\omega) = 1$) materials are considered. The linear relationship between \mathbf{D} and \mathbf{E} can also be defined using the electric susceptibility χ , which describes a linear relation between \mathbf{E} and \mathbf{P}

$$\mathbf{P} = \varepsilon_0 \chi \mathbf{E} \tag{1.4}$$

$$(\varepsilon(\omega) = 1 + \chi)$$

Finally, the last constitutive relationship relates the current density to the field through the electrical conductivity, σ

$$\mathbf{J} = \sigma \mathbf{E} \tag{1.5}$$

Traveling-wave solutions to Maxwell's equations lead to the wave equation

$$\mathbf{K}(\mathbf{K} \cdot \mathbf{E}) - K^2 \mathbf{E} = -\varepsilon(\mathbf{K}, \omega) \frac{\omega^2}{c^2} \mathbf{E} \quad (1.6)$$

in the Fourier domain. For transverse waves, $\mathbf{K} \cdot \mathbf{E} = 0$, giving the generic dispersion relation.

$$K^2 = \varepsilon(\mathbf{K}, \omega) \frac{\omega^2}{c^2} \quad (1.7)$$

$\varepsilon(\mathbf{K}, \omega) = 0$ for longitudinal waves. Therefore, longitudinal oscillations occur only at zeros of $\varepsilon(\omega)$ [2].

1.1.2 Dispersion of Light in Metals

To derive the relative permittivity, $\varepsilon(\omega)$, of an electron plasma, the Drude model of the optical response of metals is combined with the Lorentz model of dipole oscillators. The optical response of metals is produced by the oscillation of free electrons in response to the AC electric field $\mathbf{E}(t)$ of an applied EM field. The equation of motion for the electron displacement is [1]

$$m\ddot{\mathbf{x}} + m\gamma\dot{\mathbf{x}} = -e\mathbf{E} = -e\mathbf{E}_0 e^{-i\omega t} \quad (1.8)$$

where a harmonic time dependence of the driving field is assumed [2]. The second term represents the frictional damping force of the medium and no restoring force is included because only free electrons are being considered [1]. In the equation above, γ is the characteristic collision frequency of free electrons with other particles in the material, which are typically on the order of 100THz. The oscillation of the electron, $\mathbf{x}(t) = \mathbf{x}_0 e^{-i\omega t}$, is a particular solution. The actual displacement $\mathbf{x}(t)$ is obtained from substituting $\mathbf{x}_0 e^{-i\omega t}$ into (1.8). The displaced electrons contribute to the macroscopic polarization $\mathbf{P} = -ne\mathbf{x}$ (n is the electron density). Substituting the obtained $\mathbf{x}(t)$ into \mathbf{P} , and \mathbf{P} , then, into the expression for the electric displacement \mathbf{D} (Eq. 1.2) and solving for $\varepsilon(\omega)$, one arrives at the desired result,

$$\varepsilon(\omega) = 1 - \frac{\omega_p^2}{\omega^2 + i\gamma\omega} \quad (1.9)$$

the dielectric function of a metal as function of the angular frequency ω of the applied field. ω_p is

$$\omega_p = \left(\frac{ne^2}{\epsilon_0 m_0} \right)^{1/2} \quad (1.10)$$

The complex dielectric function has real and imaginary components, $\varepsilon(\omega) = \varepsilon_1(\omega) + i\varepsilon_2(\omega)$:

$$\begin{aligned} \varepsilon_1(\omega) &= 1 - \frac{\omega_p^2 \tau^2}{1 + \omega^2 \tau^2} \\ \varepsilon_2(\omega) &= \frac{\omega_p^2 \tau}{\omega(1 + \omega^2 \tau^2)} \end{aligned} \quad (1.11)$$

where the damping rate γ has been replaced by $1/\tau$, in terms of the damping time, τ . In a lightly damped system, such as a good conductor, $\gamma \approx 0$ so $\varepsilon(\omega)$ is predominantly real and

$$\varepsilon(\omega) = 1 - \frac{\omega_p^2}{\omega^2} \quad (1.12)$$

This occurs for large frequencies near ω_p . For frequencies much smaller than γ , $\varepsilon_2 \gg \varepsilon_1$ and metals are mainly absorbing with an absorption coefficient

$$\alpha = \left(\frac{2\omega_p^2 \tau \omega}{c^2} \right)^{1/2} = \sqrt{2\sigma_0 \omega \mu_0} \quad (1.13)$$

where the DC-conductivity, $\sigma_0 = \frac{ne^2 \tau}{m} = \omega_p^2 \tau \epsilon_0$ (obtained from combining the velocity form of the particular solution and Eq. 1.5), has been used. The field falls off inside the metal as $e^{-z/\delta}$, where δ is the skin depth

$$\delta = \frac{2}{\alpha} = \sqrt{\frac{2}{\sigma_0 \omega \mu_0}} \quad (1.14)$$

Typical values for δ in metals are $\sim 100\text{nm}$. The dielectric constant changes from negative to positive values as ω is swept through ω_p [2]. The conclusion is that the R of a metal is expected to be 100% for frequencies up to the plasma frequency. Indeed, for Ag (Fig. 1.1), as an example,

the IR reflectivity is almost 100% and above 80% through the visible region. The R drops distinctly in the ultraviolet (UV) region at ω_p .

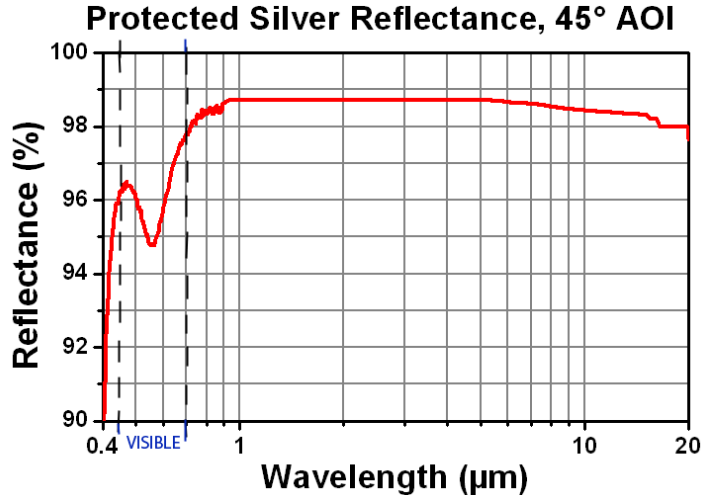


Figure 1.1: Reflectivity of silver from the infrared to the ultraviolet. The fall off is due to increased transmission, but the onset occurs at a frequency lower than ω_p due to absorption from interband transitions. Adapted from [9].

This model works for alkali metals, where ω_p lies in the UV, leading to the so-called ultraviolet transparency of metals and making them good reflectors at visible frequencies [1]. For some noble metals (Ag, Au, Cu), however, visible and higher frequency behavior is modified by interband transitions involving d electrons, limiting the validity of the plasma model [2]. These metals experience interband electronic transitions from $3d$ bands below E_F to unoccupied levels in the $4s$ band above E_F at energy differences dictated by a very high density of states (Fermi's golden rule). Metals therefore start to strongly absorb and sharply cut off the reflectivity even before ω_p . This explains why Cu and Au have a characteristic pinkish and yellowish color, respectively, but band theory is needed to explain the transitions [1]. In sum, colors are caused by interband transitions and free s electrons cause reflection.

To further illustrate the shortcomings of the plasma model, Fig. 1.2 shows the experimentally obtained real and imaginary parts of $\epsilon(\omega)$ for Ag and its plasma model fit.

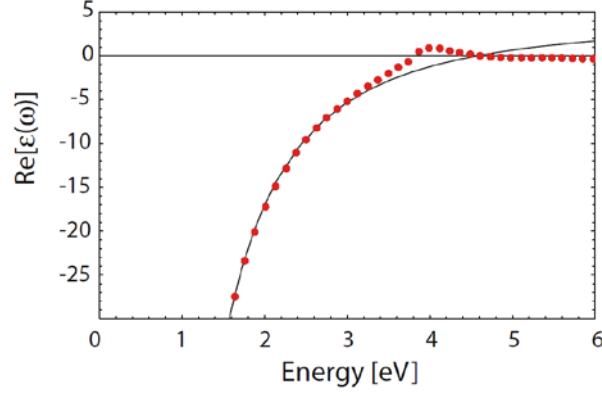


Figure 1.2: The real part of $\epsilon(\omega)$ for Ag (solid line) and a plasma model fit to the data [2].

Clearly, the model fails at higher energies due to the effect of interband transitions and a subsequent increase of ϵ_2 [2].

In the transparency regime, $\omega > \omega_p$ and at these frequencies, the conventional dispersion relation of transverse waves traveling through the electron “plasma” is obtained by using equation (1.12) in (1.7)

$$\omega^2 = \omega_p^2 + K^2 c^2 \quad (1.15)$$

This plasma dispersion is plotted in Fig. 1.3. Evidently, for $\omega < \omega_p$ there is no propagation of EM waves in the metal. For $\omega > \omega_p$, though, propagation of transverse waves is supported and the dispersion asymptotes to the light line, $\omega = ck_0$, at large wave vector.

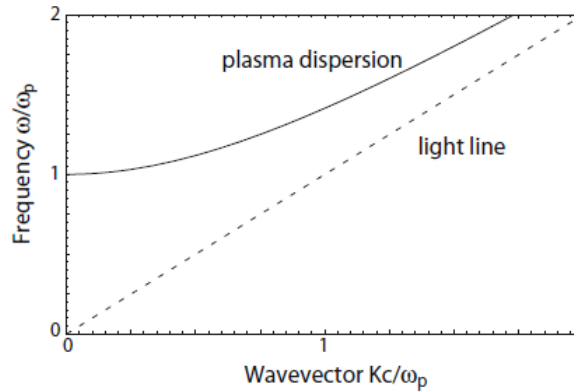


Figure 1.3: Dispersion relation of the plasma. EM waves propagate only for $\omega > \omega_p$ [2].

We have for longitudinal solutions, $\varepsilon(\omega) = 0$ ($\mathbf{K} = 0 \rightarrow$ electron oscillation is in phase), so ω must equal ω_p . This excitation is the behavior at the negligible damping limit and implies collective *longitudinal* oscillations [2]. The oscillations are dispersionless since ω is independent of \mathbf{K} [1]. These modes are called bulk or volume plasmons and are self-sustaining. They have a quantized energy $\hbar\omega_p$, just as any harmonic oscillator, typically around 10eV with a natural resonant frequency of ω_p . Light, a transverse wave, cannot directly excite plasmons since they are longitudinal oscillations. In practice, these “nonradiative” plasmons can be observed via electron energy loss spectroscopy, an inelastic scattering technique [3].

1.1.3 Surface Plasmon Dispersion

An extension of plasma physics is the concept of surface plasmons. SPs are charge density fluctuations bounded at the interface between a metal and dielectric [3]. Interest in SPs has increased rapidly in recent years, yielding a field of research called plasmonics [8]. Coupling of exciting EM radiation to these oscillations effects surface plasmon polaritons, SPPs. The dispersion relation for SPPs is found by solving Maxwell’s equations for the simplest geometry: a single planar interface (see Fig. 1.4) [2]. The confined waves propagate along the interface plane in the x direction, and the electron charge density fluctuations on the metal generate electric field lines as depicted in Fig. 1.4, in both the dielectric (positive z) and the metal (negative z). The amplitude of the electric field decays exponentially on either side of the interface [1].

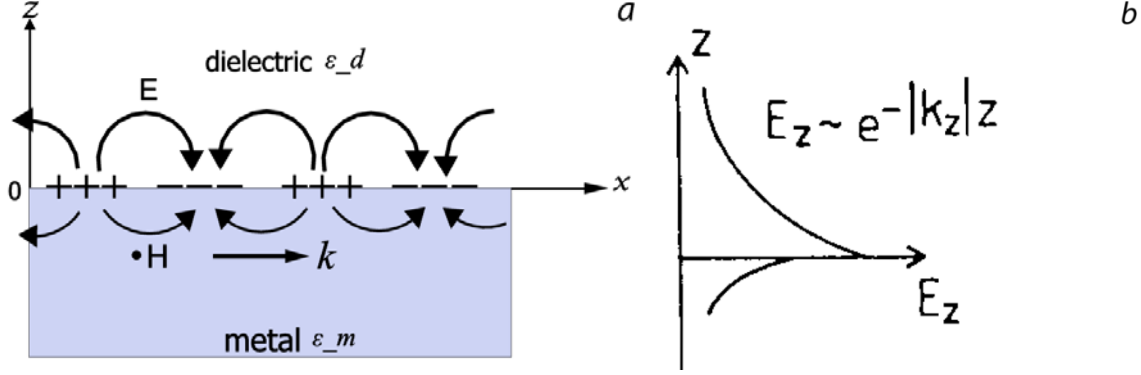


Figure 1.4: (a) Electron charge density fluctuations at the surface of a metal and the associated electric field lines. The defining axes, x and z , are also shown, along with the wave vector, k of the propagating wave. $z = 0$ defines the interface. (b) Field amplitudes decay exponentially in directions perpendicular to the interface as $\exp(-|k_z||z|)$ [3].

The dielectric is non-absorbing with a positive, real dielectric constant ϵ_d , while the conducting metal has a dielectric function $\epsilon_d(\omega)$, the real part of which must be negative. The wave equation,

$$\nabla \left(-\frac{1}{\epsilon} \mathbf{E} \cdot \nabla \epsilon \right) - \nabla^2 \mathbf{E} = -\mu_0 \epsilon_0 \epsilon \frac{\partial^2 \mathbf{E}}{\partial t^2} \quad (1.16)$$

is cast with, again, no external charge or current densities by combining the curl equations of (1.1). For negligible spatial dispersion, at least over distances of one optical wavelength ($\nabla \epsilon = 0$), and assuming a harmonic time dependence ($\frac{\partial E}{\partial t} = -i\omega$) of the electric field amplitude, the wave equation simplifies to

$$\nabla^2 \mathbf{E} + \frac{\omega^2 \epsilon}{c^2} \mathbf{E} = 0 \quad (1.17)$$

To rewrite the wave equation specifically for confined propagating waves, assume ϵ depends only on one spatial coordinate. Since waves propagate along the x direction ($\frac{\partial}{\partial x} = ik_x$) and are spatially invariant ($\frac{\partial}{\partial y} = 0$) in the perpendicular, in-plane y direction, $\epsilon = \epsilon(z)$. The wave equation now becomes

$$\frac{\partial^2 \mathbf{E}(z)}{\partial z^2} + (k_0^2 \epsilon - k_x^2) \mathbf{E} = 0 \quad (1.18)$$

($k_0 = \omega/c$, wave vector of the incident radiation). The equation for the magnetic field \mathbf{H} has a similar form. The solutions are viewed as the separate modes, TM (nonzero field components E_x , E_z , H_y) and TE (nonzero field components H_x , H_z , E_y). However, only TM modes can excite SPs because only these solutions include a nonzero E_z field component, which is the only field that can induce surface charges, thereby generating SPs. Restricting the TM solutions to the boundary conditions, which require continuity of the parallel components of \mathbf{E} and \mathbf{H} across the interface, implies that the amplitudes are equal and that the decay constants of the exponential electric field decay in the z direction must satisfy

$$\frac{k_z^d}{\varepsilon_d} = -\frac{k_z^m}{\varepsilon_m} \quad (1.19)$$

The expression for \mathbf{H} must fulfill the TM wave equation, which yields

$$\begin{aligned} k_m^2 &= k_x^2 - k_0^2 \varepsilon_1 \\ k_d^2 &= k_x^2 - k_0^2 \varepsilon_2 \end{aligned} \quad (1.20)$$

Combining the above two equations, the dispersion curve of SPPs propagating along the interface between a metal and dielectric is finally obtained:

$$k_{x,SPP} = k_0 \sqrt{\frac{\varepsilon_m \varepsilon_d}{\varepsilon_m + \varepsilon_d}} \quad (1.21)$$

k_x is the wave vector of the SPP [2]. Fig. 1.5 plots the SPP dispersion. The behavior of the SPP is different from bulk dispersion. The SPP starts at the light line of the incident dielectric medium, $\omega = ck_x/n_d$, and curves away as k_x increases, asymptotically approaching ω_{sp} , the SP frequency [6].

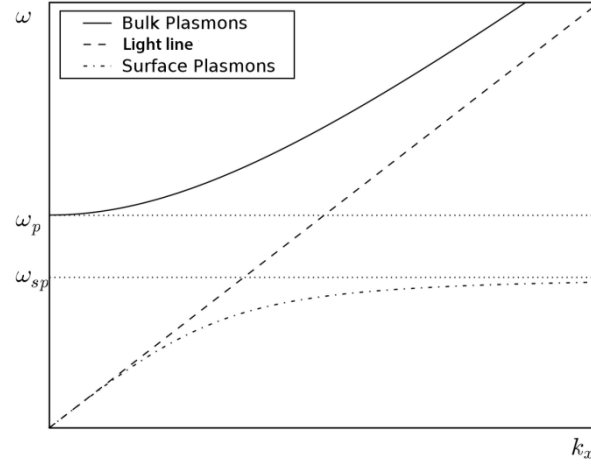


Figure 1.5: ω vs k_x for SPPs. The dispersion curve rises along the light line of the dielectric at small k_x and then turns away to asymptotically approach the cut off frequency, ω_{sp} . Since it is to the right of the light line, SPs cannot transform directly into light. Dispersion in the bulk is included for reference. Plot from [7].

At large k_x , Eq. 1.21 shows that $\epsilon_m + \epsilon_d \rightarrow 0$, so ω_{sp} can be found

$$\omega_{sp} = \frac{\omega_p}{\sqrt{1+\epsilon_d}} \quad (1.22)$$

in the limit of undamped SPPs. In the region of ω between ω_{sp} and ω_p , propagating waves are prohibited- k_x is imaginary. For $\omega > \omega_p$, radiation, unbound modes exist [1].

While the derivation of k_{SPP} concerned an ideal conductor, the dispersion relation of SPPs with Ag as the metal shows a modified behavior (see Fig. 2.4 in [2]). When there is damping, it can be seen that a maximum finite k_x is reached at ω_{sp} instead of an asymptotic approach.

Moreover, damped propagation is now allowed between ω_{sp} and ω_p [2].

There appears a trade-off between field confinement and propagation: SPPs become more localized at frequencies close to ω_{sp} (substituting (1.21) into (1.20) shows that the decay constants increase with ω), but simultaneously have a small propagation distance due to increased damping (the propagation length is affected by both free-electron and interband

damping) [1, 2]. Therefore, the main effect of interband transitions on SPPs is to increase damping and competition between the two excitations at visible frequencies [2].

1.1.4 Grating Coupling to Surface Plasmons

For the above case of a single planar interface, the SPP dispersion curve is beyond the respective light line and thus cannot be directly excited by incident light. SPPs, as their bulk counterparts, are also non-radiative modes. Light excitation requires coupling (via a prism or some kind of local scattering center) due to momentum mismatch— in the case of this thesis, a grating [10].

For a simple one-dimensional grating of “lattice” constant a , like those fabricated for the work described in this thesis (section 2.3), wave vector matching takes places when the condition

$$k_{SPP} = n_d k_0 \sin\theta \pm n \frac{2\pi}{a} \quad (1.23)$$

is satisfied [2]. The grating wave vector is $2\pi/a$, stemming from the perturbation to the smooth metal surface- it represents the periodicity of the one-dimensional lattice [3]. $k_0 \sin\theta$ is the in-plane momentum of the incoming photons, n_d is the refractive index of the dielectric and n is an integer. As will be seen in section 3.3.2, experimentally, the excitation of SPPs is detected as a minimum in the reflectivity [2]. This was first observed by R. W. Wood in 1902 and has since been named Wood’s anomaly [11]. The grating lattice points act as scattering centers, coupling light to a SP by increasing the light’s momentum by integer multiples of $2\pi/a$, the grating wave vector. The reverse process is also possible: the propagating SPs can lose an integer multiple of the grating vector and be transformed into light and thus radiate [3]. Because the periodic corrugation negates the translational invariance of the metal surface, new dispersion branches appear in reciprocal space at every multiple of the grating vector. Strictly speaking, the planar

dispersion relation no longer applies. The new dispersion relation exhibits the same translational symmetry as the surface (in the same way a Bloch function represents the periodicity of a crystal lattice) and is shown in Fig. 1.6 [4].

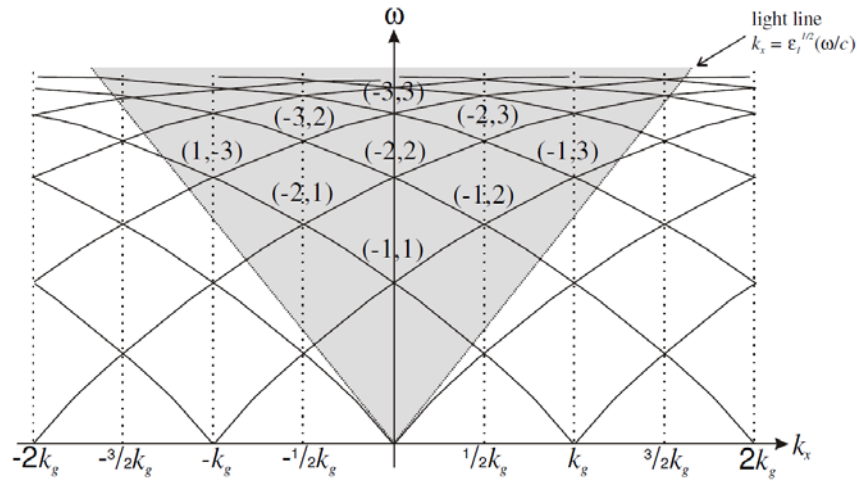


Figure 1.6: The SPP dispersion relation for coupling by a grating. The SPP dispersion relation of Eq. 1.21 has been reflected at the Brillouin zone boundaries. Light of a given frequency must intersect a dispersion branch inside the light lines for the resonance to be excited. The dispersion exists at negative and positive grating vector since the diffracted waves propagate both forward and backward. Plot from [5].

As can be seen, the effect of the grating is to fold the dispersion branches at the Brillouin zone (BZ) boundaries. The dispersion bands or branches either connect or form gaps at the BZ border, depending on the grating groove depth (the deeper the groove the more distinct the gap). Consequently, the SPP dispersion curve is physically folded into a region of ω - k space *inside* the light cone, enabling coupling to incident radiation [6].

1.1.5 Splitting of the Grating Resonance Line

One final thing to note about SPs on gratings is that the dispersion relation shown in Fig. 1.6 splits with increase in wave vector. Experimentally, the repercussion is that reflectance spectra of the gratings as a function of angle of incidence will show a single resonance line that

splits into two counter propagating SPPs as the grating is tilted about its normal axis away from normal incidence. This is, in fact, what I observed when measuring R: one red- and one blue-moving peak, which shifted symmetrically away from the single resonance position at normal incidence (see section 3.3.2). This behavior has its origin in the branching SPP dispersion relation illustrated in Fig. 1.6. This phenomenon has to be taken into account when fitting the eventual behavior of the PTCDA on grating (see section 3.3.4).

1.2 Singlet Fission

This section provides a brief overview of singlet fission (SF), a process in which the absorption of one photon can generate two electron-hole pairs in organic materials. For a more detailed treatment of SF, including a calculation of the power conversion efficiency using the detailed balance model consult [37, 39].

SF can be exploited in so-called 3rd generation photovoltaic devices, potentially doubling the quantum yield of a solar cell and allowing to surpass the thermodynamic Shockley-Queisser (SQ) efficiency limit [38]. SF was first used in 1965 to explain fluorescence quenching in crystalline anthracene by observing a dependence of its efficiency on the applied magnetic field [43]. It has since been observed in crystalline tetracene and pentacene [44-6], conjugated polymers [47-8 and others] and small-molecule carotenoids [49-50]. SF is the organic analogue of the perhaps more well-known multiple exciton generation, another carrier multiplication scheme observed in quantum dots made from, typically, colloidal lead salts [51].

SF results when a light-absorbing molecular chromophore undergoes excitation to the first excited singlet state and then shares its energy with a neighboring molecule in the ground state, creating a triplet state on each, as illustrated in Fig. 1.7. Because the two triplet excitations

produced from the excited singlet maintain an equal overall spin, SF is spin-allowed and can be viewed as a case of internal conversion- a nonradiative transition between two electronic states of equal multiplicity. A possible subsequent dissociation of the correlated triplet pair can lead to two electron-hole pairs collected per photon absorbed [37].

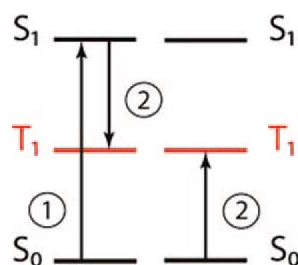


Figure 1.7: A Jablonski diagram depicting singlet fission in the simplest approximation: (1) The chromophore on the left is initially excited to S_1 and then (2) decays to yield two triplet T_1 excited states with an adjacent molecule on the right [37]. Plot from [37].

Absorber materials capable of carrier multiplication by SF following a single photoexcitation event would have a preferential energy alignment such that the excitation energy into the lowest triplet state T_1 is slightly less than half the first excited singlet energy S_1 . This ensures that the process is slightly exoergic and therefore thermodynamically favorable [37, 39-40]. The appropriate material would also exhibit singlet fission into two triplets at a rate fast enough to outcompete all other processes. These processes include electron injection into the semiconductor directly from the S_1 level, vibrational relaxation, fluorescence, relaxation to the ground state as well as the reverse process, an internal conversion back to S_1 [37, 41]. SF can, in actuality, be very fast, especially in crystalline materials where the transformation can occur on a ps or sub-ps time scale [37]. Recently, two time scales for triplet production in disordered acene films were reported to be 0.8ps and ~100ps [42]. Though the exact desired energy alignment has thus far only been observed in pentacene crystals, molecular engineering provides the promising opportunity to tailor materials with suitable SF functionality [41]. Alternatively, the goal of this

research is to utilize the strong EM field of SPs supported at the PTCDA-nanograting interface to encourage SF in PTCDA by altering its excited state energies in a favorable way. To this effect, research showing SF in perylene crystals and that perylene imides come close to the preferential energy level requirement is encouraging [41,52]. Though it has been observed in the mentioned references, the reaction coordinates of SF are poorly understood [42]. A successful outcome of this research is to gain a better understanding of the mechanism controlling SF.

1.3 PTCDA

The archetype organic semiconductor that we use is made up of a core of polyaromatic hydrocarbons functionalized with carboxylic end groups; specifically, perylene-3,4,9,10-tetracarboxylic-dianhydride (PTCDA). PTCDA is a stable organic dye and has a wide commercial use in industrial and automobile paint [20-5]. The electronic properties and structure of PTCDA have been studied in great detail [26-31].

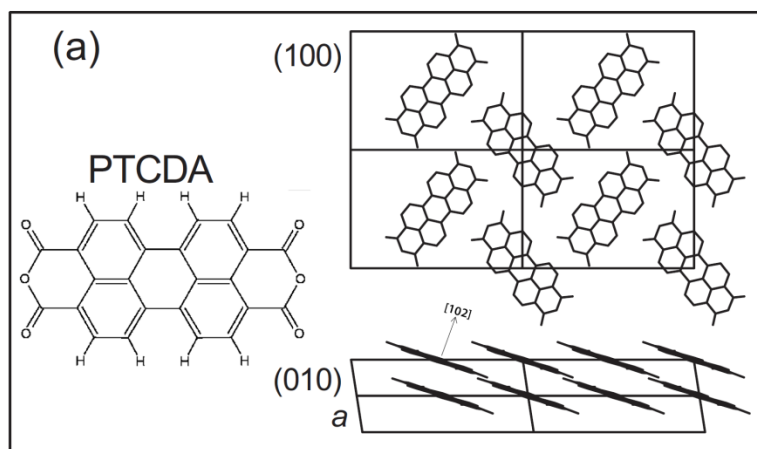


Figure 1.8: Chemical and bulk crystal structure of PTCDA. The [102] direction is perpendicular to the planes of the molecules. Adapted from [57, 63].

PTCDA's molecular structure formula is reproduced in Fig. 1.8. PTCDA crystallizes into flat stacked molecular sheets, with molecules in a sheet interlocking in a herringbone

arrangement, bonded by van der Waals forces [33]. Stacking exhibits large π -overlap with a very small interplanar distance, $d_{(102)} = \sim 3.22 \text{ \AA}$, about three times less the intermolecular distance between molecules within a stack [20,31,58]. Such tight packing with large intermolecular overlap, highly unusual for a one-component system, seems to favor charge transfer along the stacking direction and lends PTCDA its semiconducting properties. Interactions in other directions are weak [30,36]. This organic semiconductor is a model system for study of molecular excitation in organic crystals because it readily forms well-ordered single crystalline films in organic molecular beam- or quasi-epitaxy, especially necessary for measurement of transport phenomena [20,28]. Molecules generally align conveniently parallel to the substrate surface [31]. The regular, simple and tight packing structure also makes it convenient for theoretical modeling [29]. Due to its large electron affinity, this perylene derivative exhibits p-type semiconductivity in a donor-acceptor couple [29, 34].

It is generally agreed that the absorption spectrum of PTCDA originates from a mixture of Frenkel (FE) and charge-transfer (CT) exciton contributions as well as low-energy states. Specifically, the peak around 2.25 eV is a free CT-dominated state while the broad band around $\sim 2.6 \text{ eV}$ is a mixed CT-FE state dominated by a vibronic progression [31]. Excitations in PTCDA are described in more depth elsewhere [26-7, 29-31, 36], but this terminology is pertinent for the fitting of the absorption spectra when PTCDA is deposited on top of our gratings, described in section 3.2.

Our PTCDA, obtained from Acros Organics, was deposited either on microscope glass slides as witness films for absorption measurements or on the grating samples. Glass substrates were cleaned prior to deposition in heated acetone and IPA baths, with sonicating in between. This was followed by a DI H_2O rinse and drying under a stream of N_2 . The films were prepared

by thermal evaporation at a chamber pressure in the low 10^{-6} mbar range and a growth rate of $\sim 1 \text{ \AA/s}$ as determined by a quartz crystal oscillator. For determination of absorbance values for different film thicknesses, films of 5, 10, 20, 40 and 100nm were prepared (thicknesses were verified by atomic force microscopy). The absorbance spectra of these films are shown in Fig. 1.9 and agree well with data in literature. As seen in Fig. 1.9, the expected characteristic features are a high magnitude two-peak structure in the 400-600nm spectral portion.

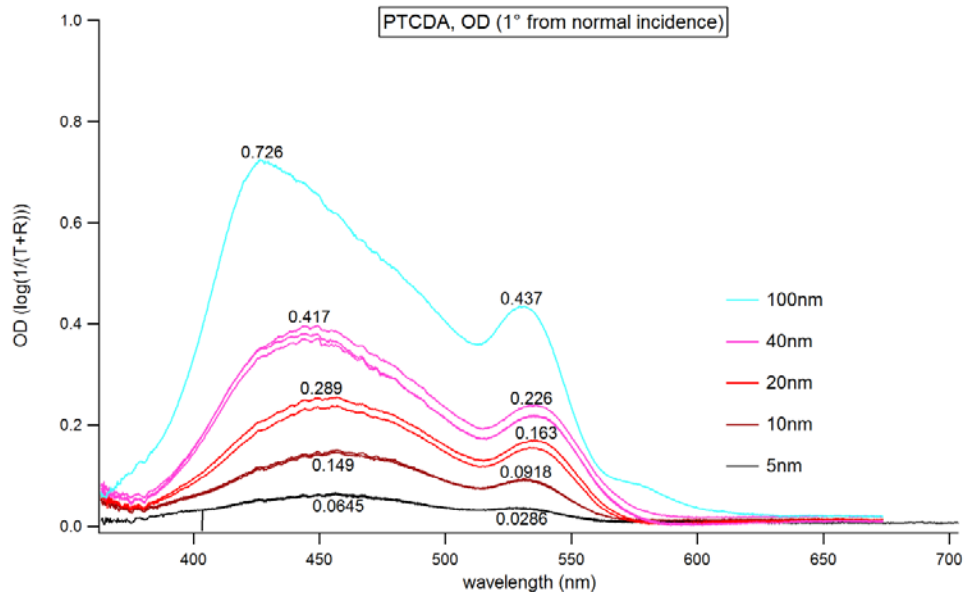


Figure 1.9: Linear normalized absorption spectra of PTCDA films of varying thicknesses. Absorbance or optical density (OD) values shown on the plot are for the two peak positions: a broad band at $\sim 2.6\text{eV}$ (475nm) and a sharp feature around 2.25eV (540nm). Measured 24-36 hours after deposition. (Note: These absorbance spectra were calculated using both transmittance and reflectance spectra for each sample, but, since scattering is not taken into account, they would more accurately be described as extinction spectra.)

Based on the first fitting results with 20nm PTCDA on top of the grating, 10nm films were decided upon as the preferred thickness for the grating samples to make the amplitudes of the PTCDA and grating features comparable. The grating resonance was tuned to overlap with and enhance the CT-dominated peak of PTCDA at 2.25eV ($\sim 550\text{nm}$).

For reference, Fig. 1.10 shows the reflectance spectra of a PTCDA film on Ag backing substrate overlaid with the reflectance of one of our (bare) gratings. It shows that we were able to achieve gratings with a resonance that directly overlaps the relevant PTCDA excitation to produce enhanced excited state absorption.

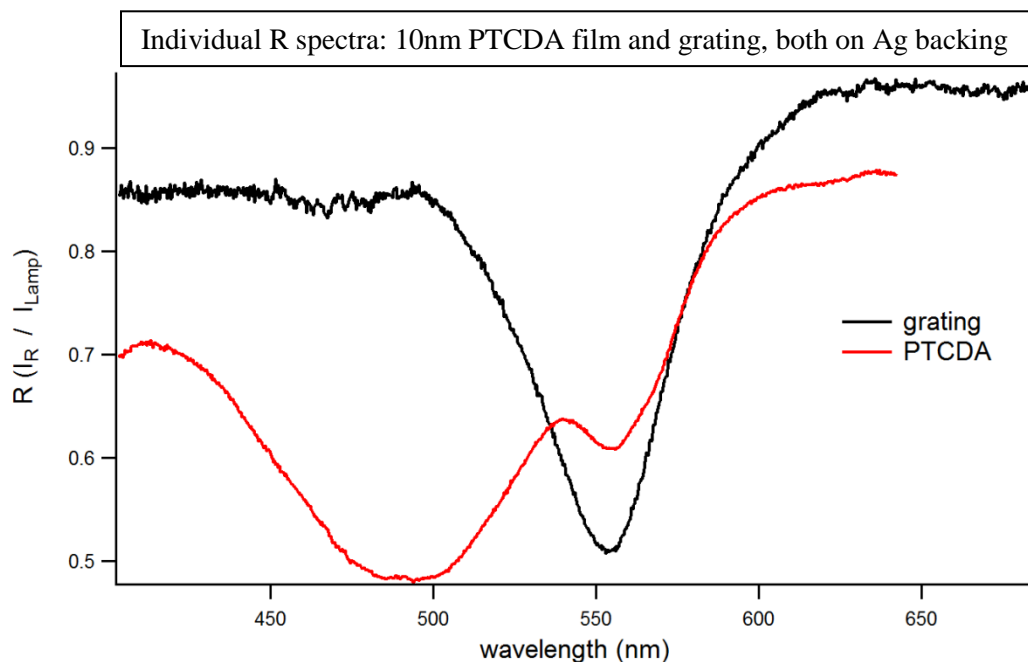


Figure 1.10: Reflectance of bare a bare 10nm PTCDA film and a bare grating. The SP resonance is shown to overlap directly with the CT-dominated peak in PTCDA.

Chapter 2

Fabrication of Gratings

Grating samples for the research presented in this thesis were fabricated by two lithographic techniques: first with laser interference lithography (LIL) and later with nanoimprint lithography (NIL).

2.1 Laser Interference Lithography

I started with laser interference lithography because the setup was already functioning and in-use within the lab for other projects. A schematic of the LIL setup is shown in Fig. 2.1. In the LIL setup, a monochromatic, spatially coherent laser was guided by optical components (mirrors and beam splitter) onto the sample slot. A spatial filter expanded the beam as well as allowed the removal of high frequency noise, providing a clean Gaussian profile [13, 19].

LIL is a maskless lithographic technique. The working principle is based on the interference of two coherent, obliquely incident light beams (achieved via a beamsplitter in our setup) to produce interference fringes, recorded in the photoresist-coated substrate [12, 13]. The setup used in the work for this thesis easily yielded $\sim 1\text{cm}^2$ of patterns with great ordering [14]. The period of the standing wave interference pattern and, thus, of the resulting grating is dependent on the incident wavelength, λ , and the half angle of the intersection of the two beams, θ , as illustrated in Fig. 2.2 and shown in Eq. 2.1. [13]

$$P = \lambda / (2 \sin \theta) \quad (2.1)$$

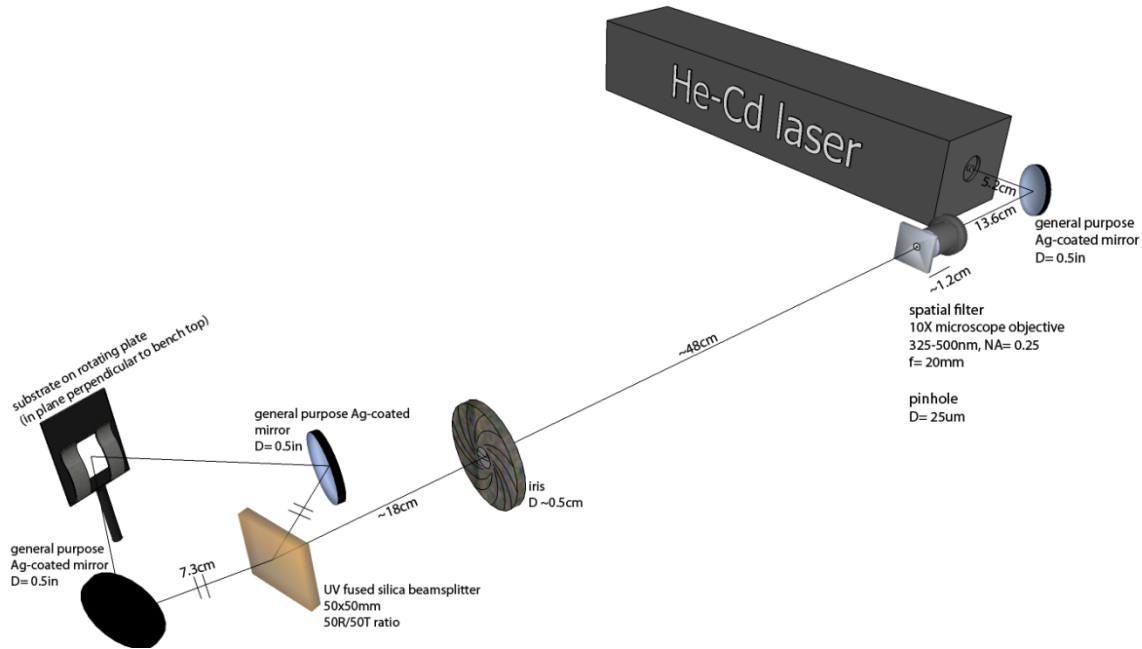


Figure 2.1: Schematic of the two-beam laser interference lithography setup used for the fabrication of gratings for the research described in this thesis.

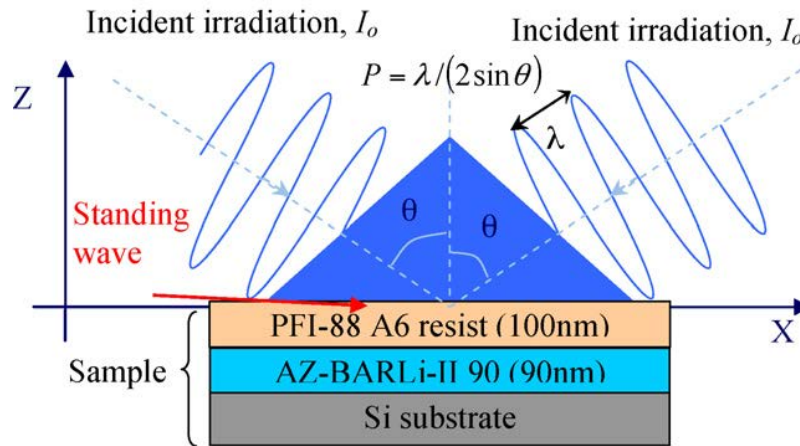


Figure 2.2: The standing wave of two beam interference holography with a beam splitter. Diagram from [13].

In practice, θ was calculated from the known illumination wavelength and desired periodicity, as shown in Fig. 2.3. Then, the distances between beamsplitter, mirrors and substrate were adjusted as accurately as possible to satisfy the necessary θ .

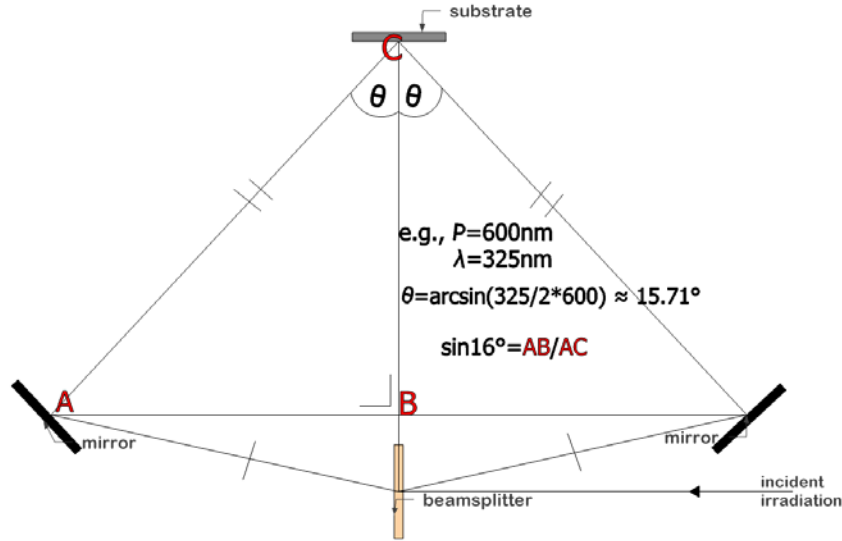


Figure 2.3: Optical layout of two-beam LIL showing how we determined the correct arrangement for a certain desired periodicity, P , knowing: the irradiation wavelength, λ , and the half-angle of interference, θ .

As seen in Fig. 2.3, if we chose 600nm for the desired periodicity with an illumination wavelength of 325nm, then the half angle of the intersection of the two beams is known and mirrors and sample holder are moved accordingly.

Since the spatial period of the grating can be as low as half the incident wavelength, structures on the order of 100nm are achievable from deep UV light [15] (though exposure time also affects the final size of the features). Both one-dimensional and two-dimensional periodic patterning is possible with LIL by interference of multiple beams or rotation of the sample when only two beams are used. Geometries range from lines or grooves (1D) to a grid of rounded pillars/dots/holes (2D) and even some polygonal shapes depending on the resolution the resist can uphold and exposure conditions. Though achievable features are not as diverse in shape as

with other techniques, LIL makes use of simple equipment, allowing it to be a low-cost alternative to the more popular and expensive electron (e-beam) and focused ion beam (FIB) lithographies [13]. Another great advantage over e-beam and FIB is scalability. The patterned size depends on the interference area, how close to the spatial filter the aperture is located and the coherence length of the laser. A typical gas laser, HeCd for example, has a fairly large, >30cm, coherence length and, combined with simple optics, could make gratings on a much larger scale [18]. Yet a third advantage is the speed of patterning, which depends on the exposure time, which, in turn, is a matter of choosing the appropriate resist type. Negative resists tend to pattern faster than positive: typically, exposure times are on the order of seconds vs. minutes.

In our setup, we used a Helium Cadmium Laser from Kimmon Electric/Koha Co., Ltd (IK5551R-F) at the 325nm line, 15mW, TEM00 mode, beam diameter, $d = 1.1\text{mm}$. The spatial filter was made up of a 10x microscope objective lens (Thor Labs LMU-10X-NUV, $f = 20\text{mm}$) and a $25\mu\text{m}$ diameter pinhole. The pinhole was matched to the objective by the following formula [16]:

$$\text{pinhole diameter} = \frac{8}{\pi} \times \frac{\lambda * f}{d} = \frac{8}{\pi} \times \frac{325\text{nm} * 20\text{mm}}{1.1\text{mm}} \cong 15\mu\text{m} \quad (2.2)$$

In practice, a slightly wider pinhole is preferable to avoid aberration effects, so we used the $25\mu\text{m}$ -diameter pinhole [17]. The distances from the spatial filter to the exposure area were far enough to ignore beam divergence and result in a large enough exposed area [18]. The sample holder, beam splitter, mirrors and all other components were centered on the optical axis.

The fabrication protocol used a negative-tone resist, half-diluted SU-8 2000.5 (diluted with SU-8 Thinner- cyclopentanone), with a preliminary layer of OmniCoat to improve resist stripping off the soda-lime microscope glass substrates. OmniCoat was spin-coated in two steps at 500rpm for 5s followed by 3000rpm for 30s. The substrate was then baked at 200°C for 60s.

After the sample cooled to room temperature, SU-8 was coated also in two steps: first at 500rpm for 5s followed by 4500rpm for 30s. The substrate was then baked at 95°C for 45s. The appropriate light dose required to neither under- nor overexpose the resist was determined from trial runs of grating fabrication of varying exposure times. A 15-20s exposure time was settled on for SU-8— much less sensitive to laser power fluctuations than positive-tone resists which have longer exposure times, on the order of minutes. Following exposure, the sample underwent a post-exposure anneal at 95°C for 1.5min to reduce resist solubility in the developer. Wet development (removal of unexposed resist with a liquid; as opposed to dry development with a gas) followed and was done in SU-8 developer (PM acetate) for ~45s-60s. Un-exposed photoresist was descummed via a reactive ion etch (RIE) with oxygen plasma for <10s. Metal (Ag) deposition was carried out via thermal evaporation at pressures in the mid to low 10^{-6} mbar range. Subsequently, lift-off was done in Remover PG under sonication at 80°C for ~10min. I switched to SU-8, after unsuccessful lift-off using positive resist AZ1505. Negative resists are more stable against the myriad of exposure and development conditions, have lower exposure times and generally produce more sharply defined features. The parameters of the above-described LIL procedure using SU-8 resist were developed over numerous trials seeking to perfect the grating quality and resulted in eventual reproducibility of successful lift-off and gratings with resonance at the desired position (see section 2.3). All chemicals were from MicroChem. We achieved a total oval-shaped patterned area of about 4cm by 8cm, of which approximately 75% was well ordered and showed the expected dip in reflection spectra.

The most important drawback to the existing LIL setup was that any change in desired periodicity required inconvenient adjusting of the incidence angles of the two beams separately. This involved miniscule tweaking of both mirrors and sample holder and was prone to

introducing differences in intensity between the two beams at the exposure slot. A Lloyd's mirror setup would have avoided this by using a single mirror mounted perpendicular to the sample holder, as in Fig. 2.4.

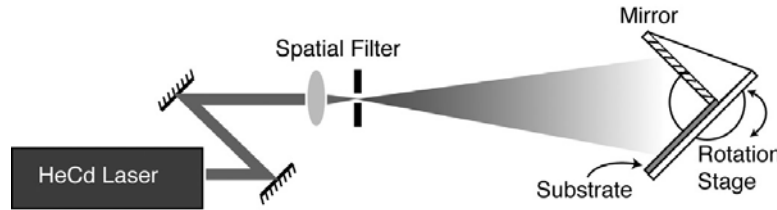


Figure 2.4: Schematic of a Lloyd's mirror interferometer. Diagram from [15].

One beam is the original beam reflected off the mirror and the other is the original laser beam itself. The period of the interference pattern is still given by Eq. 2.1, but since the reflecting mirror is attached perpendicular to the substrate, θ is equal to the stage rotation angle read off from the stage mount. This allows for easy pitch adjustment by rotating the mirror/substrate setup about its center point. In addition, the mechanical rigidity of this assembly due to the close proximity of mirror and substrate makes it less sensitive to vibrations between interfering beams [18].

Ultimately, the LIL process, though theoretically straightforward, was not so in practice. Constant laser power fluctuations made consistency between successive sets of gratings made with the initial positive-tone resist impossible. Its exposure times of 3-12min were likely long enough to effect non-uniform exposure over the interference area. I eventually pinpointed the source of fluctuations to an unstable mounting of the spatial filter. Grating quality improved drastically after switching to SU-8 and remounting the spatial filter on a more stable, rigid mount. I was able to achieve gratings with the desired and expected optical characteristics. That is, with grating resonance at the correct wavelength, as predicted by simulations (see section 2.3 for SEM images). However, the setup was cumbersome to adapt for fabrication of a new grating

structure that included a metal backing underneath the grating (new simulations showed an even higher still absorption enhancement for this structure). The light dose had to account for light now reflecting off the substrate instead of transmitting through (as before, when the resist was just on a glass substrate without a backing). The NIL process was in place for other projects in the group, so grating fabrication switched to fabrication by NIL.

2.2 Nanoimprint Lithography

The process of nanoimprint lithography is illustrated in Fig. 2.5 below. Nanoimprinting follows the same general set of steps as other lithographic techniques (in parenthesis):

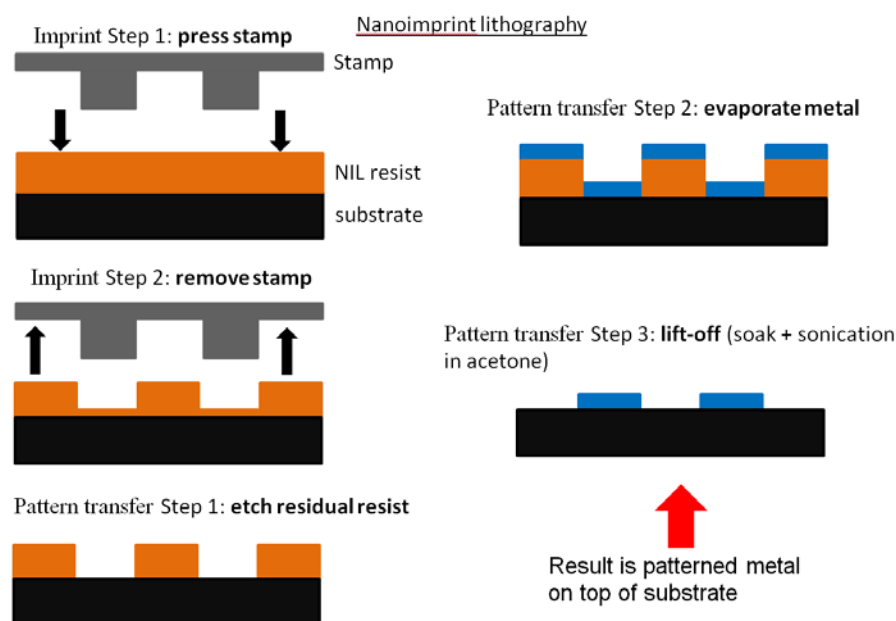


Figure 2.5: Step-by-step diagram of the nanoimprint lithographic process.

1. Cleaned substrate is coated with resist or imprinting medium (same)
2. Cleaned mold is coated with anti-stick layer (a clean mask, for example, if photolithography)
3. Substrate is imprinted (if photolithography, sample exposed with the mask pattern)
4. Underprinted resist is descummed with a reactive-ion etch (underexposed resist is descummed)
5. Metal is deposited (same)
6. Lift-off is done on the remaining resist to achieve patterned metal on substrate (same)

Nanoimprint proved to be the more reliable method. Any change in periodicity, though more expensively than with LIL, was accommodated with the purchase of a new stamp of appropriate dimensions. Of course, the NIL process posed its own difficulties. Examples included dealing with imprinted resist sticking to and coming off with the mold (required pre-coating the mold with an anti-sticking coating), pressure non-uniformities during imprint causing subsequent variations in RIE conditions and the relationship between substrate thickness and size of uniformly imprinted area. These issues were dealt with either in the preliminary testing or as they came up without much hindrance to the flow of sample fabrication. For example, probable oxidation of the underlying Ag backing layer during RIE was eliminated by incorporating an additional 10nm Au layer between the backing and the grating since Au does not oxidize. Also, uniformity in pressure over the imprinted area during imprinting was improved by switching to a thinner substrate (a silicon wafer instead of microscope glass slides). These issues and others were confronted, as well as all of the NIL fabrication carried out, by Lisa Rengnath of Electrical Engineering in collaboration with Zhen Wang from Mechanical Engineering, both at CU-Boulder.

In the long run, NIL was a cheaper, and often more reliable, lithographic technique than others available, such as e-beam or FIB. Upfront costs, though, were comparable since the stamps or molds are fabricated by these exact techniques. Our samples had a patterned area of 6x6mm. However, just as LIL, NIL is also scalable since it is possible to use the biggest mold available (500 μ m by 500 μ m) with e-beam and then stamp it many times on one substrate. Unlike LIL, this technique is not limited to periodic 1D and 2D rectangular feature geometries since the shape is dictated by the mold and virtually any arrangement is possible with molds made by, for example, e-beam. Another advantage principle to this research was the ease of accommodating

changes in periodicity or feature dimensions, as highlighted above. The limiting factor was the purchase of new molds of appropriate dimensions. Though these can be quite expensive, the fabrication process remains the same with the new mold.

2.3 Evaluation of Gratings

This chapter summarizes the results of grating fabrication with LIL in a chronological manner. During fabrication, grating quality was assessed via scanning electron (SEM) and atomic force microscopy (AFM) imaging and by taking absorbance spectra. AFM images were generally taken immediately following resist patterning to determine if exposure was successful enough to continue with the lithographic process, while SEM images and optical spectra were taken after lift-off on finished gratings. The goal of this chapter is to summarize a process that led to current grating fabrication by NIL. SEM images of the gratings are presented as visual support.

I started fabrication with laser interference lithography of a 2D grating whose parameters are summarized in the table below.

dimension	pitch (nm)	feature size (nm)	feature depth (nm)	resist	metal
2D	270	100	30	+	Au

Table 2.1: Grating dimensions with which I started grating fabrication by LIL. Gratings were 2D- an array of holes in Au.

The parameters were chosen according to results from finite element simulations in COMSOL as the best configuration for absorption enhancement. The grating thickness, 30nm, is in the scale of optical penetration depth. The hole size is considerably smaller than half the periodicity, with a duty cycle of $100\text{nm}/270\text{nm} = 37\%$. Still, with the LIL setup arranged for the correct

periodicity (see Fig. 2.3 in section 2.1), I decided the hole size could be reduced by slightly overexposing the sample. Once the appropriate resist thickness accounting for an eventual 30nm deposition of metal was determined, fabrication proceeded as per the procedure explained in section 2.1, describing resist coating, exposure, etc. Fig. 2.6 presents SEM images of a grating made with parameters of Table 2.1. First, image (a) shows that I was able to achieve a regular periodic exposure of a 2D array. Analysis of the feature dimensions shows that I achieved correct periodicity with a variation of $\pm 10\text{nm}$ and that the features have an average width of $\sim 160\text{nm}$. Notably, though, the features are mounds instead of holes, which indicates improper lift-off or even lack thereof. Knowing that the deposited Au was 30nm in thickness gives an estimate of about $\sim 160\text{nm} - 30\text{nm} = \sim 130\text{nm}$ for my resist mounds, which suggests that the resist mounds were not quite as small as I was targeting. Hole dimensions measured in (f) agree. Ideally, the metal coats only the tops of the resist mounds and the exposed glass around them. With 2D features made of positive resist, however, the side walls of the features tend to be rounded due to the sinusoidal nature of the incident interfering light intensity and become coated overall during metal deposition, making lift-off hard. Still, as seen in (e) and (f) of Fig. 2.6, some regions, about 1-3% of the entire patterned area, did have proper lift-off.

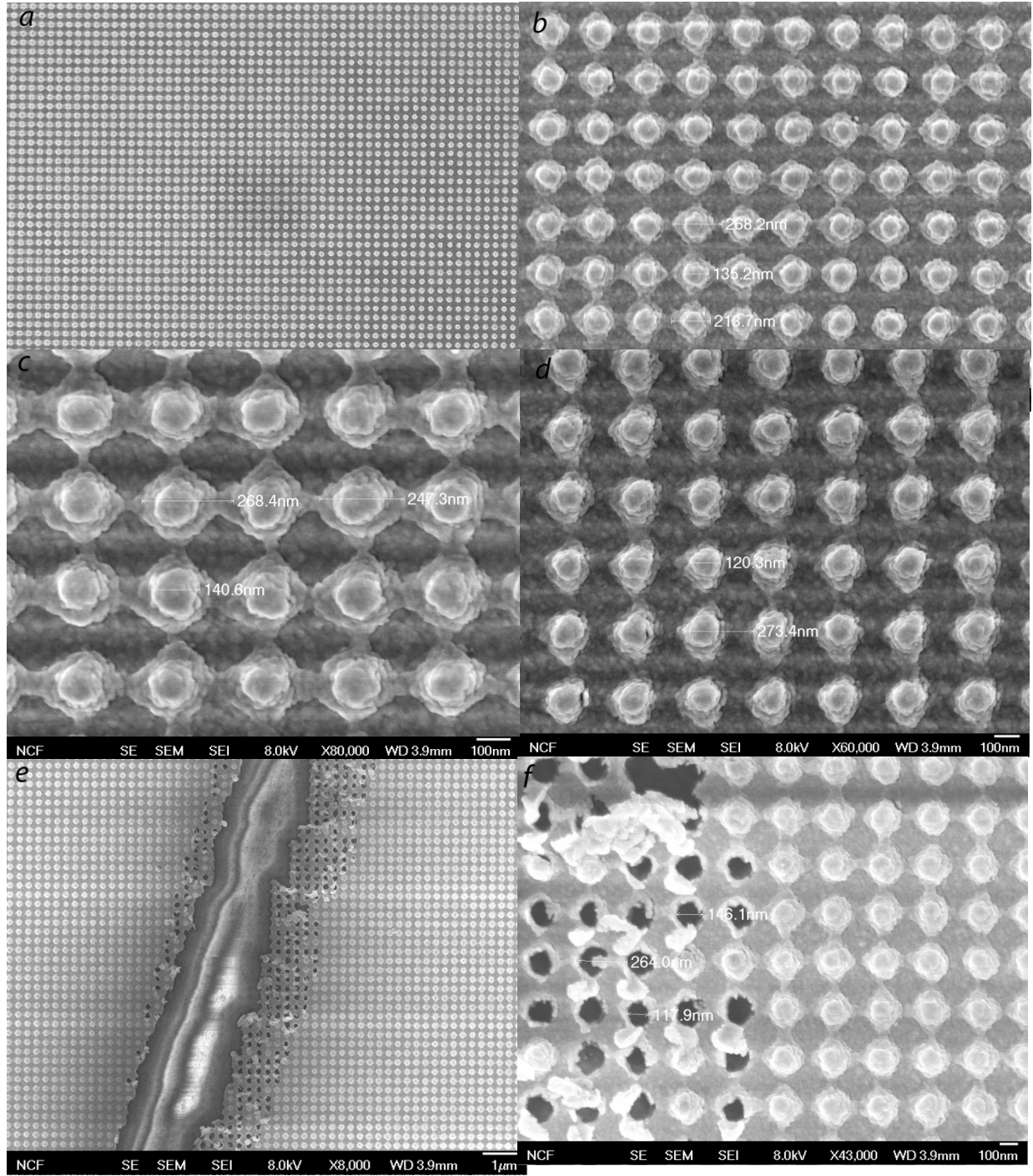


Figure 2.6: SEM images of some gratings of a set made with the parameters as in Table 2.1. For clarity, the measurements shown on the SEM images are listed here. (b), (c), (d) show mound dimensions: 135.2nm, 213.7nm, 140.6nm, 120.3nm; and pitch measurements: 268.2nm, 268.4nm, 273.4nm. (f) shows hole dimensions: 117.9nm and 146.1nm; and pitch: 264.0nm.

To try to improve solvent penetration on these same gratings, I used a more rigorous lift-off method after the above SEMs were taken. Soaking overnight was added, followed by brief heated soaking and a switch to a stronger lift-off agent, Remover PG (sonication continued as before). These gratings were then imaged again and those images are gathered in Fig. 2.7. The new lift-off method helped in so much as the regions with proper lift-off increased to about 3-4% of the patterned area. A new issue observed in this bout of imaging, displayed in (a) of Fig. 2.7, were the perplexing regions of what seems to be uniform Au with neither mounds nor holes. A cause for this could have been that the mounds were displaced before Au deposition, but I would have seen this under AFM and I did not. It was likewise not observed under SEM the first time before Remover PG use (from Fig. 2.6 to Fig. 2.7). Alternatively, the resist mounds were perhaps so shallow in these regions that the deposited Au covered them in a smooth layer. This point seemed unlikely since I optimized the resist deposition to give a thickness of at least three times the Au thickness (130-140nm). Such shallow mounds also seemed highly unlikely on such a large scale.

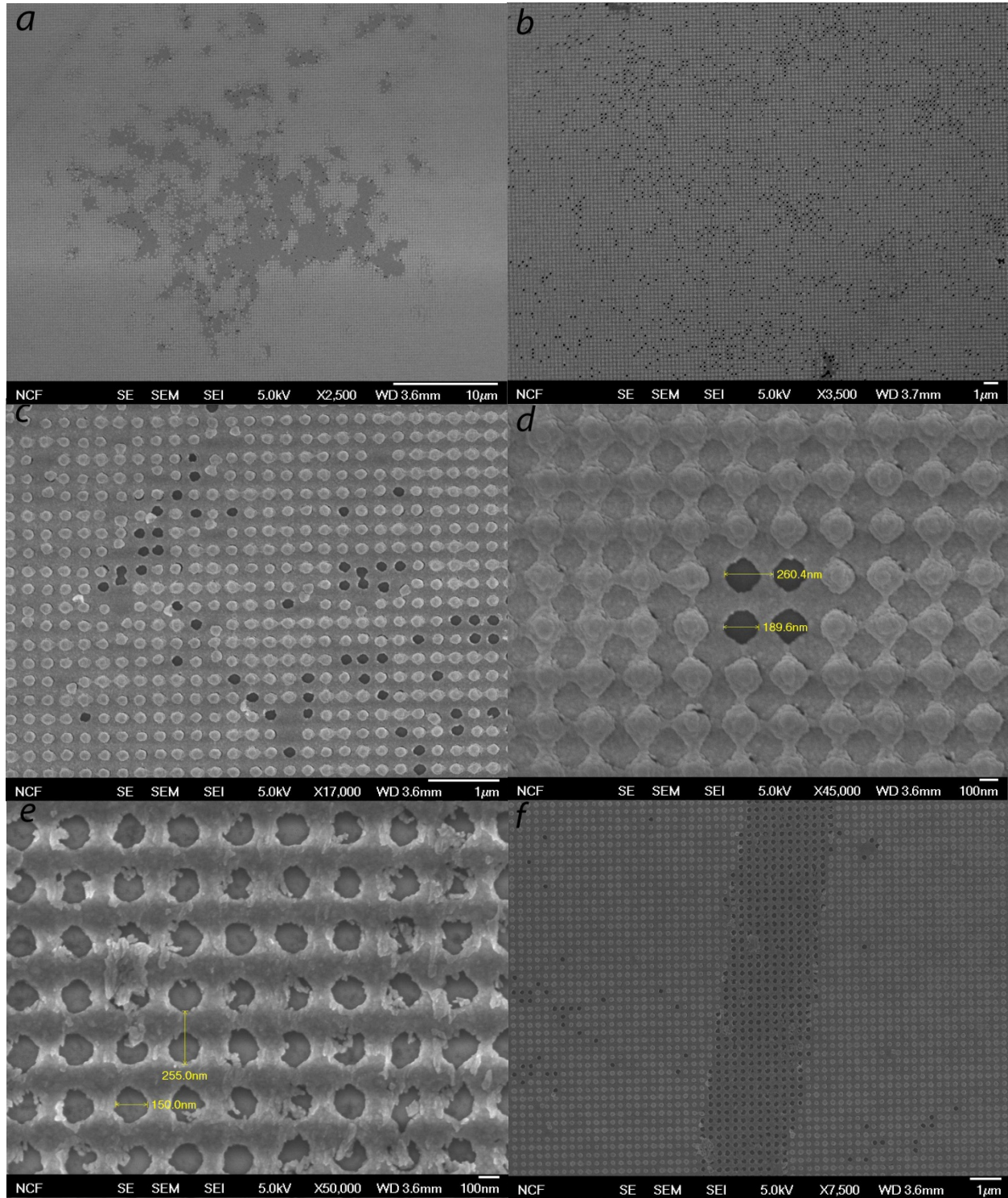


Figure 2.7: Gratings of the set presented in Fig. 2.6 after a second round of lift-off with the more rigorous conditions mentioned: soaking in PG Remover overnight, followed by heated soaking at 75°C followed by sonication as before. In (d), pitch: 260.4nm and hole diameter: 189.6nm. In (e), pitch: 255.0nm and hole diameter: 150.0nm. (c) and (d) are zoomed in areas of (a) and (b) and (e) is a magnified area of (f).

Another issue of note with imperfect lift-off was the poor adhesion of Au to glass that caused entire patterns to come off during sonication.

One more round of fabrication was undertaken with a slightly altered fabrication procedure, considering all that was learned from the first sets of gratings. Specifically, a 2nm layer of Cr was evaporated before the Au to improve Au adhesion to glass. The sample was also not rotated during Au deposition to encourage one-sided coating of the mounds to have a better chance of solvent penetration during lift-off. Likewise for this aim, a thinner, 20nm layer of Au was deposited. Grating dimensions remained as in Table 2.1 and lift-off was done in the latest, more rigorous way. Fig. 2.8 shows these SEM images.

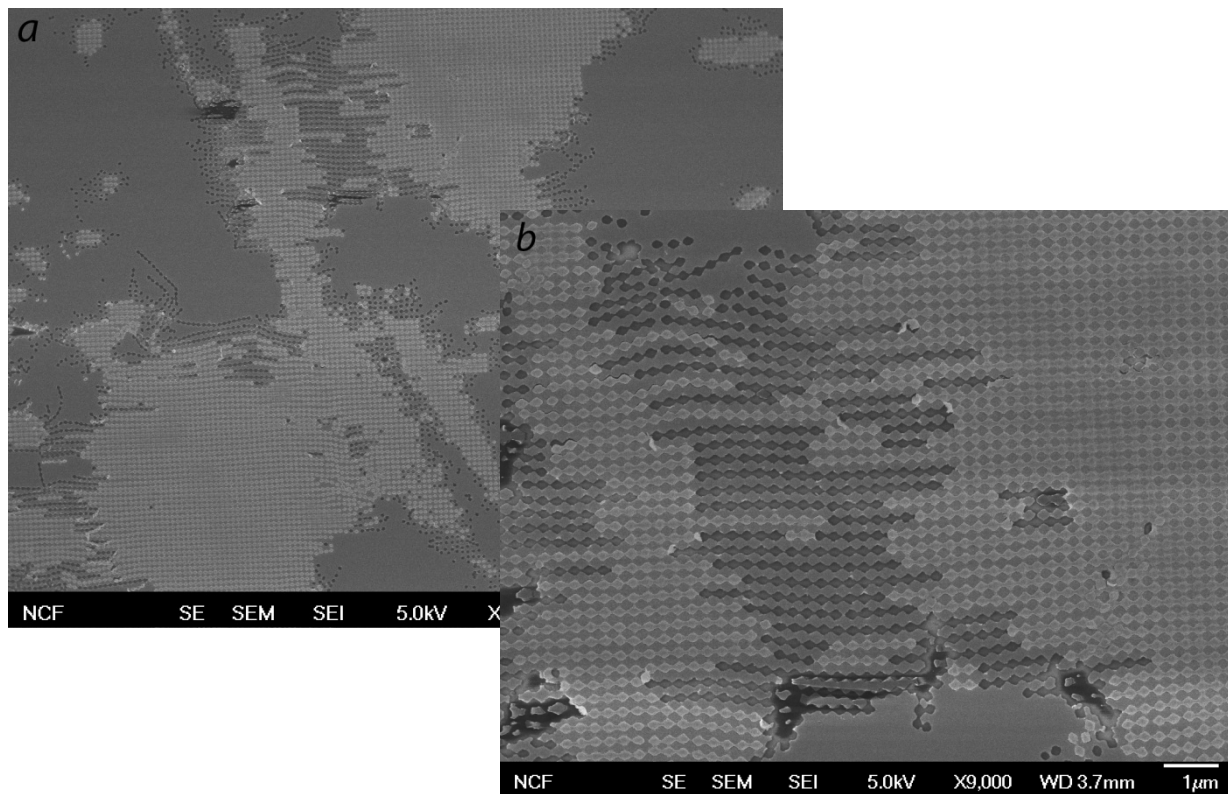


Figure 2.8: SEM images of another set of gratings fabricated with dimensions shown in Table 2.1, 2nm of Cr deposition before Au, 20nm instead of 30nm of Au, no sample rotation during metal deposition and the more rigorous lift-off process. In effect, these gratings were expected to have good lift-off considering the improvements made to the lithographic process as compared to previous samples (Fig. 2.7). Both images show large areas of neither mounds nor holes. (b) is a zoomed area of (a).

Dimension analysis again showed that the desired periodicity was achieved. There were also more holes seen than in the previous set of gratings, so, in this sense, lift-off improved with the slightly altered procedure. The additional Cr layer also helped as I was able to sonicate longer without having the entire pattern dislodge. However, there were also more of these regions with neither mounds nor holes.

In light of the underwhelming success of the altered procedure which included all plausible changes, we decided to switch from fabrication of 2D holes in Au to 1D lines of Ag. The new parameters are summarized in Table 2.2.

dimension	pitch (nm)	feature size (nm)	feature depth (nm)	resist	metal
1D	270	110	20	+	Ag

Table 2.2: Grating dimensions after the switch from 2D to 1D features. These were lines of Ag on glass and the second type of grating I fabricated with LIL.

Most notable is that the 1D grating introduced more relaxed fabrication constraints: one exposure instead of two, a much better adhesion of Ag to glass and a duty cycle now within, albeit just barely, the 40-60% feasible range. However, unsuccessful lift-off continued after numerous trials of making gratings with these new parameters likely due to, at least in part, the drifting laser alignment problem. A visual survey of typical gratings during this period is provided in Fig. 2.9.

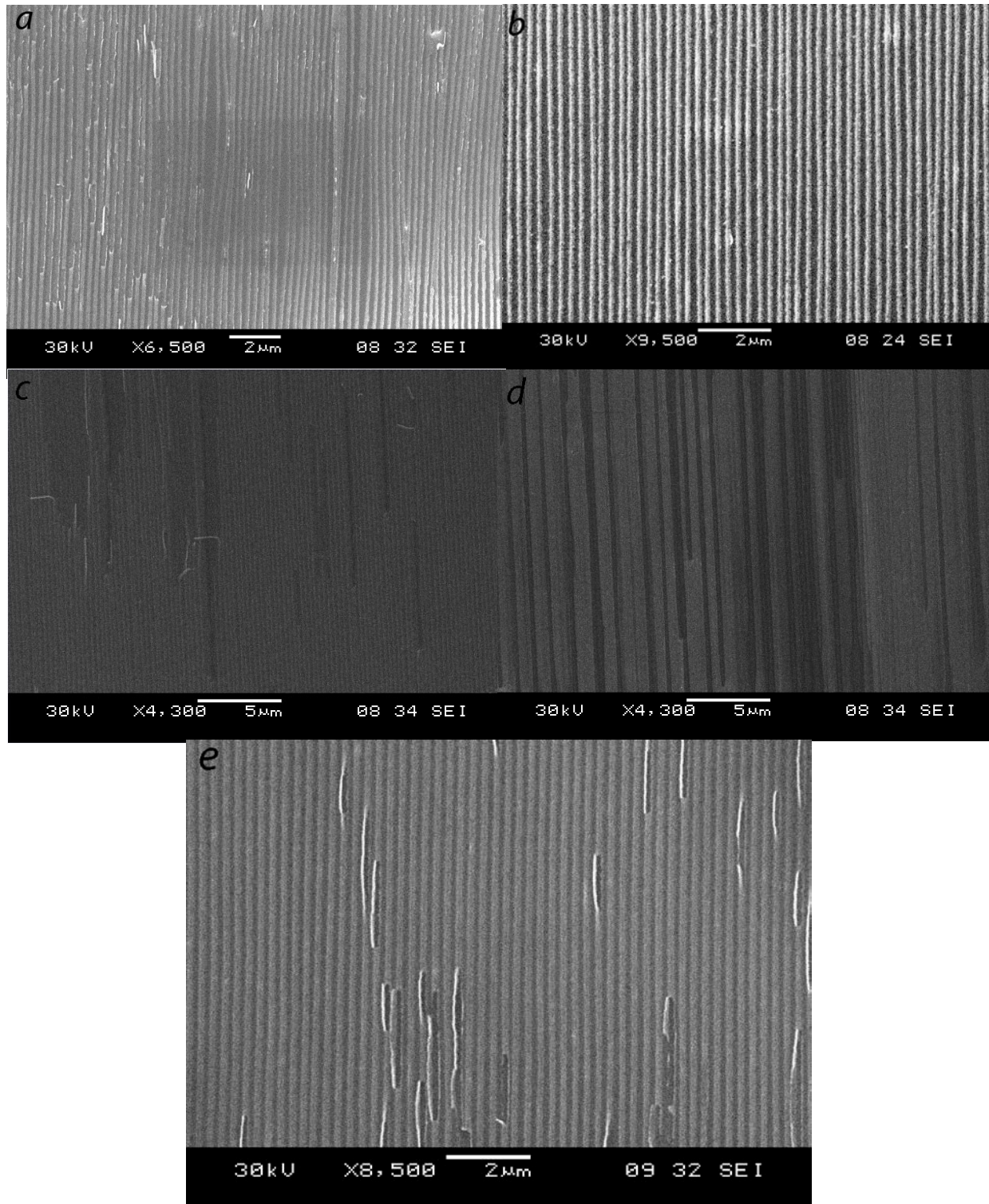


Figure 2.9: SEM images of the 1D gratings. Lines in (a) are not straight and there is a large distribution of line width, (c) shows lines stripping off from the substrate. In (e), regions where parts of lines have come off can be seen.

After remounting the spatial filter, switching to negative resist and light-dose testing to determine new exposure times (for SU-8), I finally produced gratings with successful lift-off. They also revealed a grating resonance in the desired position, as compared to simulations. I was also able to reproduce these successful results in multiple subsequent sets of grating fabrication. SEM images of these good gratings are presented in Fig. 2.10. As can be seen, the lines are for the most part straight and uniform throughout the patterned area and one can imagine a clean square-wave grating profile. Analysis of grating dimensions was likewise encouraging: over 11 samples, line width was $113\text{nm} \pm 11\text{nm}$ and pitch was $272\text{nm} \pm 6\text{nm}$ – in line with the target parameters of Table 2.2. A sample transmittance (T) spectrum of one of these good samples is reproduced in Fig. 2.11. Here, there is a dip in T instead of R because these gratings did not have a backing to reflect incident light— instead, glass for its transmission. This particular grating showed a resonance at $700\text{nm} \pm 50\text{nm}$ for T spectra taken at multiple spots of the entire patterned area. Such an uncertainty was typical for all the gratings of the third type. The resonance is very broad but wide enough to overlap with the 550nm peak of PTCDA and potentially effect absorption enhancement. New simulations, however, were showing an even greater absorption enhancement for gratings fabricated on a thick metal (Ag) surface instead of directly on the glass. I started dose testing trials to determine exposure time with these new backing-included gratings but, as mentioned in section 2.1, the NIL process was in place so grating fabrication by LIL was not continued.

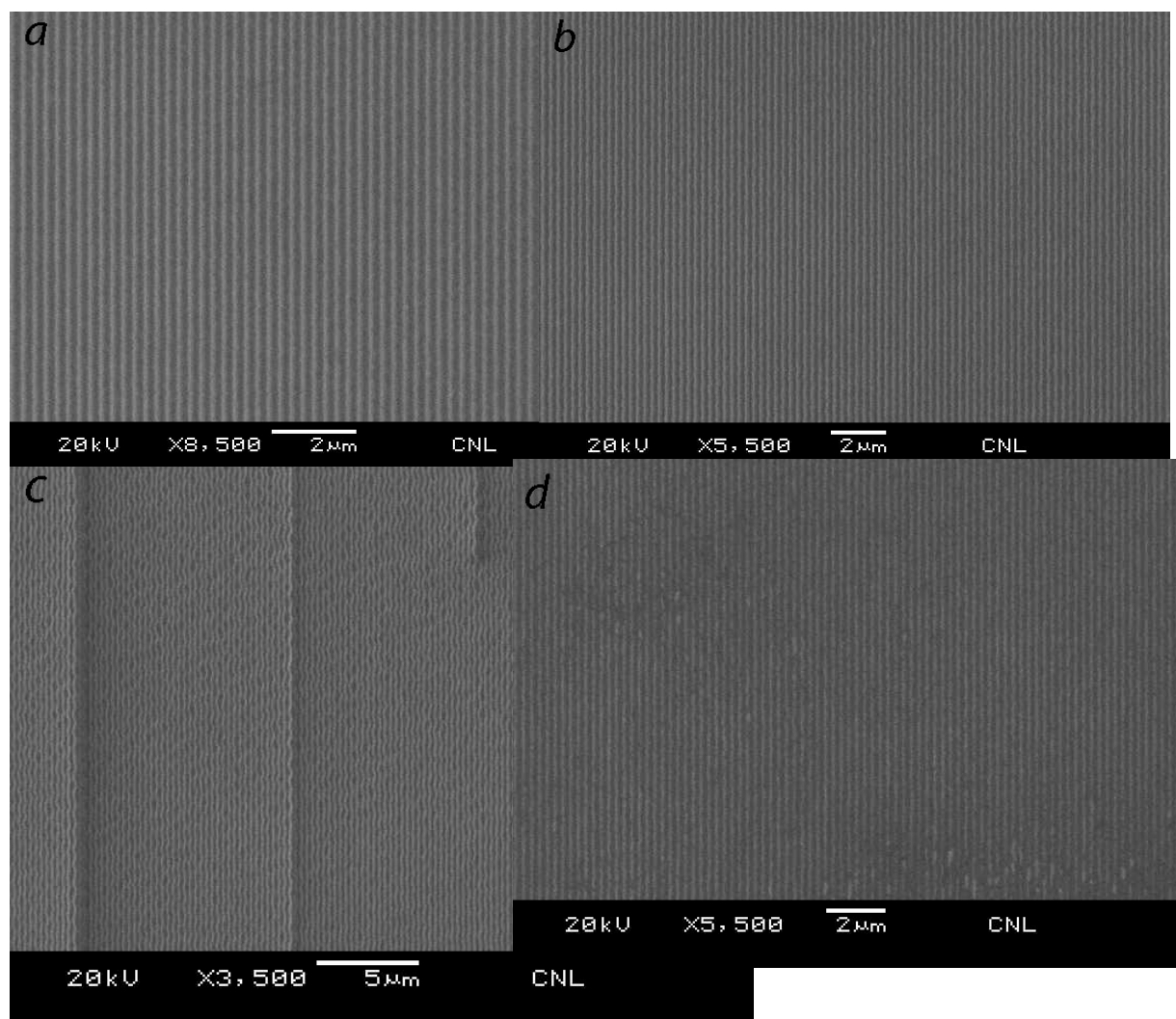


Figure 2.10: SEM images of gratings with good lift-off that I was able to achieve after switching to negative resist. Lines are seen to have clean lift off, are straight and with high range of good ordering. Waviness to the lines, as in (c), was also occasionally observed.

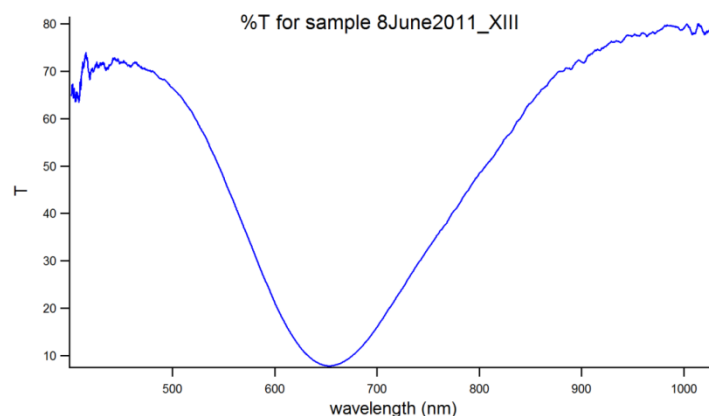


Figure 2.11: A sample transmittance spectrum for the gratings of the third type, with good lift-off.

Chapter 3

Assessment of Surface Plasmon Effect

This chapter presents the beginning efforts of assessing the effect of surface plasmons on the molecular photophysics of polycrystalline PTCDA. First is a description of the spectrometer-like setup built to characterize the gratings. Following is an explanation of the customized global fitting procedure written to ground the experimentally measured optical spectra with data from the literature. The last part of the chapter is dedicated to a discussion of the fits obtained for bare PTCDA, bare grating, grating+dielectric spacer and, finally, grating+dielectric spacer+PTCDA.

3.1 Angle-Resolved, Variable Polarization Transmission/Reflection Setup

The motivation to build an angle-resolved transmission (T) and reflection (R) setup with a variable polarization capability came from a finite-difference time-domain simulation revealing anticrossing behavior of SPs with molecular excitons of PTCDA. Fig. 3.1 plots the dispersion curve for PTCDA on the nanograting. In the absence of a grating resonance, the conventional absorption peaks of PTCDA do not shift with a changing angle of incident light— solid horizontal lines in Fig. 3.1. However, the addition of the grating response, that which red-shifts with angle of incident light (section 1.1.5), causes the $\sim 2.25\text{eV}$ CT exciton peak in PTCDA to slightly redshift along with the SP resonance— blue triangles curve. Assuming the resonances overlap exactly at normal incidence, this anticrossing behavior disappears within the first few ($\sim 5^\circ$) angles of incidence, after which the conventional behavior resumes: the PTCDA exciton peak is stable, while the SPP (green triangles) continues to redshift, now, at a slightly faster rate.

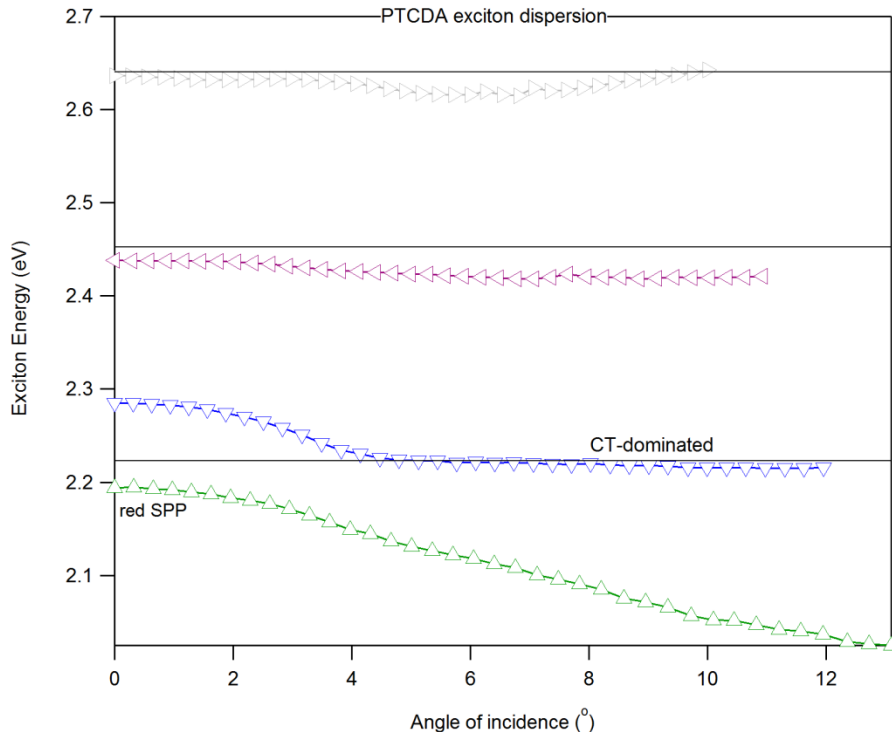


Figure 3.1: Anticrossing behavior between the structural (grating) and absorption (PTCDA) resonances as a function of the angle of incidence. The lowest horizontal black line depicts the conventional behavior of the CT-dominated exciton peak in PTCDA (no shift with incident angle). The blue-triangle curve depicts the behavior with the addition of the grating (slight redshift and then stable). The red-moving grating resonance is the green-triangle curve which first red-shifts in unison with the PTCDA peak as it sweeps through it and then shifts faster. An important feature, which to notice, is the split between the coupled SPP-like and CT-like at zero incidence. This separation of ~ 0.1 eV is called Rabi splitting: it is due to the nature of the coupling. In fact, such a splitting is evidence of coupling [64].

In order to observe this behavior experimentally, the angle-resolved T/R setup, Fig. 3.2, was built. It is capable of, at least, 0.5° resolution. For R measurements, the large concave mirror accepts angles as close as 1° from normal incidence up to $\sim 12^\circ$. The angle of incidence is changed by rotating the substrate stepwise around its normal axis. The variable polarization capability allows characterization of the grating without exciting SPs and therefore T/R spectra normalized to the Ag backing layer (which, for example, levels the sloping background due to scattering). I would not have been able to achieve these same capabilities on existing equipment

because reflection measurements were either not a possibility or the light incidence was fixed at 8° off from normal and too large to detect any potential anticrossing of the PTCDA excitation.

Angle-resolved reflectance spectra were taken for all samples for both horizontally and vertically polarized incident light in the spectral range $\sim 400\text{-}700\text{nm}$ at the following angles: 1° , 2° , 3° , 4° , 5° , 6° , 7° , 8° , 9° , 10.15° and 11.3° . For all samples, data was obtained from multiple regions of the patterned area.

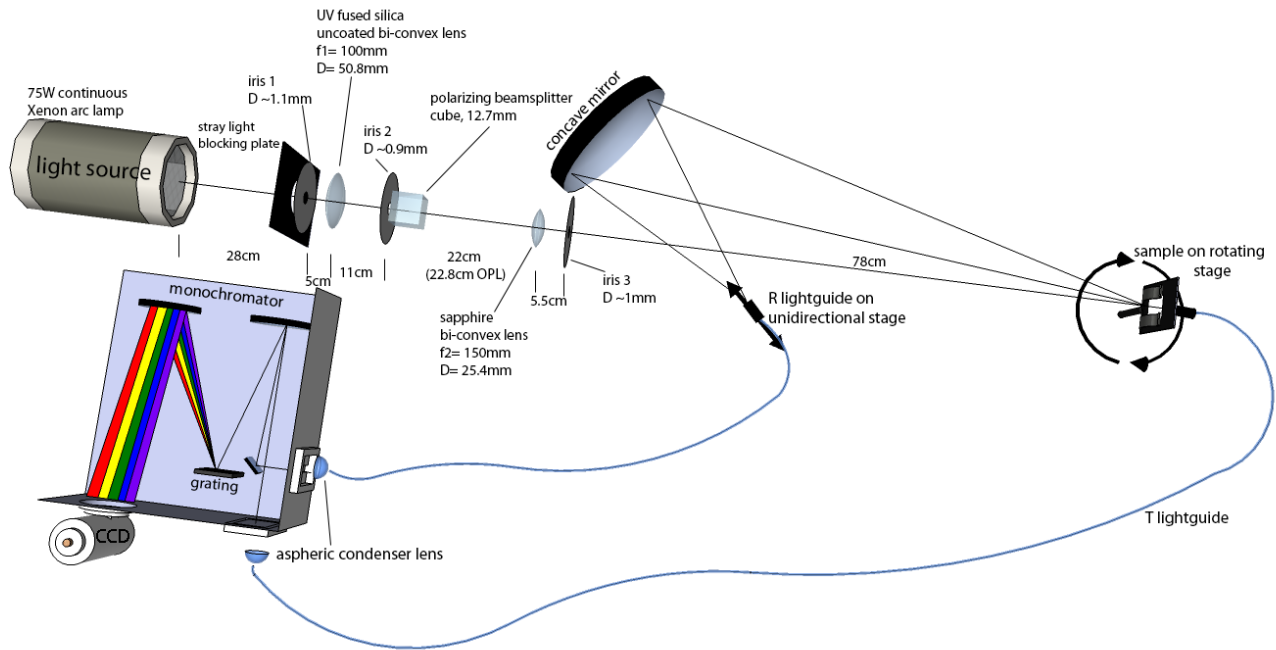


Figure 3.2: Angle-resolved, variable polarization reflection/transmission setup. The light source is a continuous Xenon arc lamp. Reflected/transmitted light is collected and guided to the monochromator and CCD detector inside light guides.

3.2 Fitting Procedure

A reduced chi-squared global fit procedure was developed for fitting experimental reflectance spectra of thin-film PTCDA on plasmonic nanogratings in order to quantify any indications of exciton/plasmon coupling and their anticrossing interaction. The procedure,

particularly the part concerning the spectral contribution of the organic chromophore, delves into the dynamics of electronic processes in organic crystals. I first provide a curt summary of some properties of optical transitions as necessary to elucidate the terminology used in explaining the fitting procedure, followed by a description of the fitting procedure itself.

When a molecule absorbs a photon, its transition dipole moment describes the charge redistribution between the initial and final states over both the nuclear and electronic coordinates. In the Franck-Condon approximation, electronic transitions occur on a short time scale, $\leq 10^{-15}$ s, as compared to $\sim 10^{-13}$ s for nuclear motion [62]. The energy associated with the extent of geometrical rearrangement of the nuclei between the upper and lower states is represented in a fundamental quantity termed the Huang-Rhys factor, S . It naturally comes out from expressing the transition dipole moment as an integral over the initial and final state wave functions and separating these into electronic and nuclear or vibrational parts. A transition from the zeroth vibrational level in the ground state to the zeroth level in the excited state, the zero phonon line, corresponds to a Huang-Rhys factor of 0— the arrangement of the ground and excited electronic states is identical so no relaxation between vibrational states occurs and the transition is purely electronic. Higher values of S correspond to a distribution of vibronic states. The resulting absorption band consists of a progression of transitions between these consecutive vibronic subbands, differing in energy by the vibrational quantum, $\hbar\omega$. These transitions can be said to occur at the zero, first, second, etc. phonon lines. The number of vibrational states that have significant enough overlap to contribute to the overall electronic transition are finite. Quantum theory explains why the intensities of the individual phonon lines depend on the overlap of the vibrational wavefunctions of the initial and final electronic states. The envelope of the individual

intensities of these different phonon lines, each with its own probability, predicts the overall continuous spectral absorption band shape for the molecular crystal [60-2].

The global fit procedure combines the spectral contributions of thin-film PTCDA and grating. The PTCDA contribution can be decomposed into the CT-dominated and other excitons. The broadband at ~2.6eV mixed CT-FE electronic transition of PTCDA as a vibronic progression of five subbands, where each higher subband has less spectral weight. Each subband of the vibrational manifold is represented by a normalized bell Gaussian line shape multiplied by the Franck-Condon factor, $S^n e^{-S}/n!$, for the particular phonon mode:

$$\text{VibMan}_n = -AS^n \frac{e^{-S}}{n!} \frac{1}{\sigma_n \sqrt{2\pi}} \exp\left(-\frac{1}{2} \left(\frac{x - (E_{00} + (n \cdot \hbar\omega))}{\sigma_n}\right)^2\right) \quad (3.1)$$

The Franck-Condon factor represents the transition to the particular phonon mode, i.e., zeroth, first, etc. A is the amplitude, S is the electron-phonon coupling constant for bulk PTCDA, integer n is the n th phonon mode, E_{00} is the position of the zero phonon line, x is the energy in eV and $\hbar\omega$ is the aforementioned vibrational quanta. The negative sign fits the dips in the reflectance spectra. The user inputs a width, γ_n , from which the standard deviation, σ_n , for the Gaussian is calculated by

$$\sigma_n = \frac{\gamma_n}{\sqrt{8 \ln 2}} \quad (3.2)$$

The term $1/(\sigma_n \sqrt{2\pi})$ makes the Gaussian unitary (its integral over its full domain is 1 for every σ_n). Five of these lineshapes were used with $n = 0..4$. A value of 0.8-1 was used for S and $\hbar\omega$ was initially set to 17meV. These values were obtained from the literature for solution PTCDA (not thin-film) [58-9]. The total vibrational manifold is the sum of the five Gaussians.

The 2.25eV CT-dominated state as well as a lower energy peak around 2eV were modeled as purely electronic transitions, represented by the Gaussian,

$$CT_state = -\frac{A_{CT}}{\sigma_{CT}\sqrt{2\pi}} \exp\left(-\frac{1}{2}\left(\frac{x-E_{CT}}{\sigma_{CT}}\right)^2\right) \quad (3.3)$$

(The expression is the same for the lower energy peak with parameters specific to it). The CT peak is linked to the vibrational manifold by a shift from E_{00} , $E_{CT} = E_{00} - \Delta E_{CT}$. The sloping background, most likely caused by scattering, has a λ^{-4} dependence,

$$background = y_0 - \frac{K}{\lambda^4} = y_0 - \frac{K}{\left(\frac{ch}{q} \frac{1}{eV}\right)^4} \quad (3.4)$$

where c is the speed of light, h is Planck's constant, q is the elementary charge, K accounts for the degree of sloping in the background and y_0 is the scaling factor. All lineshapes have adjustable positions, widths and intensities.

The grating contribution to the global fit model involves two normalized Lorentzian lineshapes that are allowed to move symmetrically away from the position, E_0 , of the single resonance line at almost normal incidence (1°) as the incident angle is increased:

$$grating\ resonance_{b,r} = -\frac{A_{b,r}}{\pi\gamma_{b,r}} \frac{1}{1 + \left(\frac{x - (E_0 \pm (\text{slope} * \theta^\circ))}{\gamma_{b,r}}\right)^2} \quad (3.5)$$

The subscripts b and r denote the blue-moving and red-moving peaks, respectively, as the resonance line splits with incident angle. The $+$ sign is for the blue-moving peak while the $-$ sign corresponds to the red-moving peak. $A_{b,r}$ is the area and $\gamma_{b,r}$ is the width of the respective peak.

The lineshapes' separation is constrained to be linear with angle of incidence, $\Delta E = \text{slope} * \theta^\circ$.

This relation was determined from individual fits of each R spectra at each angle for the first gratings obtained. The lineshapes are allowed to have different widths and areas, though they are maintained nearly identical and they are linked to be the same for all angles. The total fit is the sum of the PTCDA and grating contributions. All the freely adjustable parameters of the model are gathered in Table 3.1.

Background	offset, y_0
Background	Prefactor, K
Vibrational Manifold	Amplitude, A
Vibrational Manifold	Energy, E_{00}
Vibrational Manifold	phonon quantum, $\hbar\omega$
Vibrational Manifold	Huang-Rhys, S
Vibrational Manifold	Width0
Vibrational Manifold	Width1
Vibrational Manifold	Width2
Vibrational Manifold	Width3
Vibrational Manifold	Width4
Charge-Transfer	Amplitude, A_{CT}
Charge-Transfer	ΔE_{CT}
Charge-Transfer	Width_CT
Low Energy	Amplitude, A_{LE}
Low Energy	E_{LE}
Low Energy	Width_LE
Grating Resonance	Area r
Grating Resonance	Area b
Grating Resonance	E_0
Grating Resonance	γ_r
Grating Resonance	γ_b
Grating Resonance	Slope of ΔE

Table 3.1: The freely adjustable parameters of the global fit procedure to fit reflectance spectra of PTCDA on grating.

Evidence of anticrossing behavior between the SPs and the PTCDA excitons would show a shift of the position of the PTCDA CT-dominant peak in unison with the moving position of the grating resonance, as obtained from the global fits of the reflectance spectra of PTCDA on grating. The quality of the fit is evaluated visually by considering the size of uncertainties in the parameter values and, finally, the size of χ^2 .

3.3 Fits

3.3.1 Bare PTCDA

10nm PTCDA was deposited on a substrate of the base structure of the grating samples: 200nm Ag + 40nm Cr + <100>Si (Cr is included only to make the Ag surface smooth). R spectra for vertically polarized light for a sample of PTCDA on Ag+Si are presented in Fig. 3.3

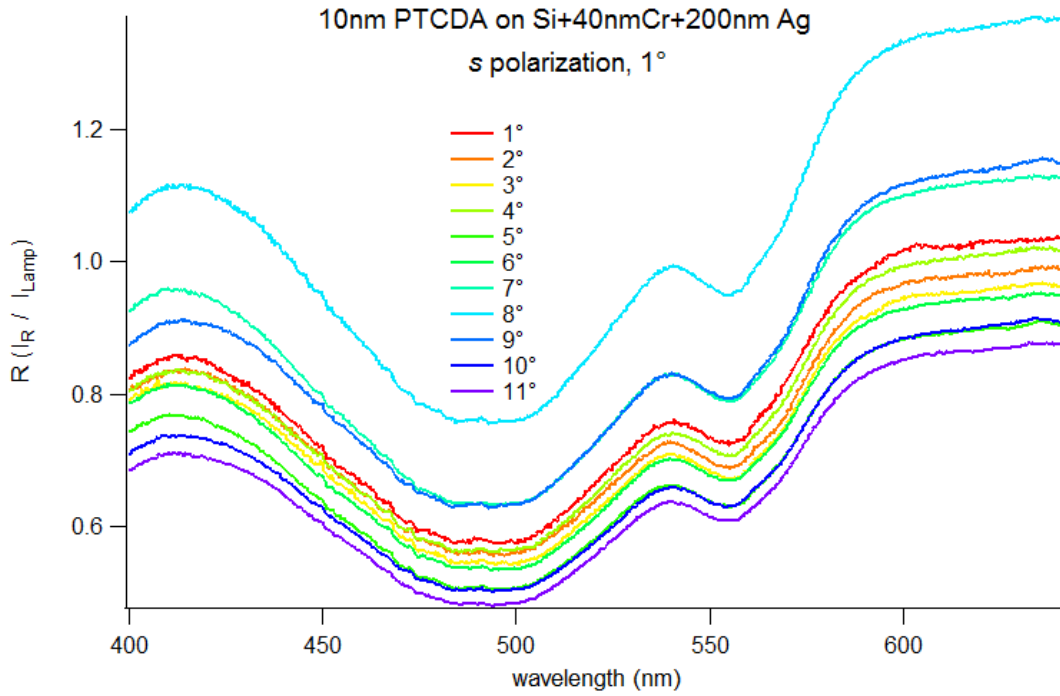


Figure 3.3: R spectra of 10nm PTCDA on 200nm Ag + 40nm Cr + Si for the incident angle range indicated (with respect to normal, 0°, incidence) and vertically (s) polarized light.

All angles were fitted as described in section 3.2 using just the PTCDA contribution code. An example fit for 1° is shown in Fig. 3.4.

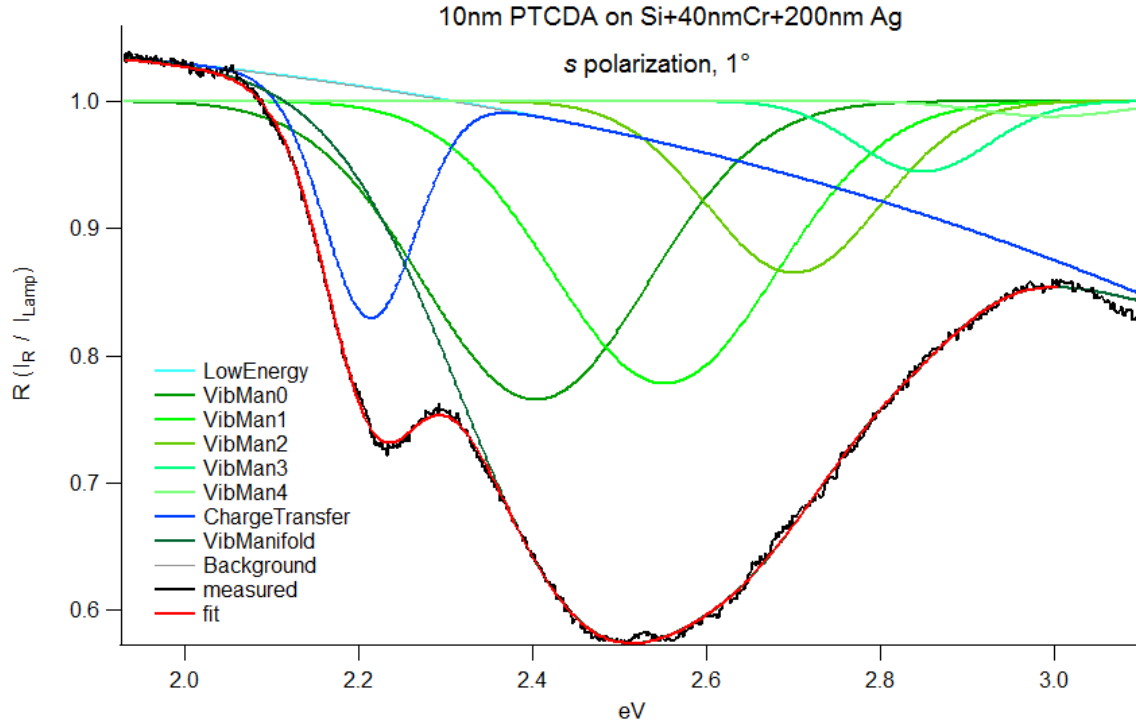


Figure 3.4: Fit to experimental R spectrum for 10nm PTCDA on 200nm Ag + 40nm Cr + Si for 1°. Parameters are: $E_{00} = 2.40\text{eV}$; $\hbar\omega = 0.15\text{eV}$; $S = 0.94$; width0-4: 0.305, 0.303, 0.233, 0.178, 0.190; $A_{CT} = 0.0238$; $\Delta E_{CT} = 0.191$; width $_{CT} = 0.123$; $A_{LE} = 0.0005$; $E_{LE} = 1.86\text{eV}$; width $_{LE} = 0.19$.

The fits are in good agreement with measured spectra. It is evident from the value for its amplitude that the low energy peak has a very small contribution to the overall fit. The parameters obtained here were used as the starting values for fitting the R measurements of PTCDA on grating in section 3.3.4.

3.3.2 Bare Grating

Sample bare grating reflectance spectra of one grating for the smallest and largest angles are reproduced in Fig. 3.5 to show the characteristic splitting of the resonance line with angle.

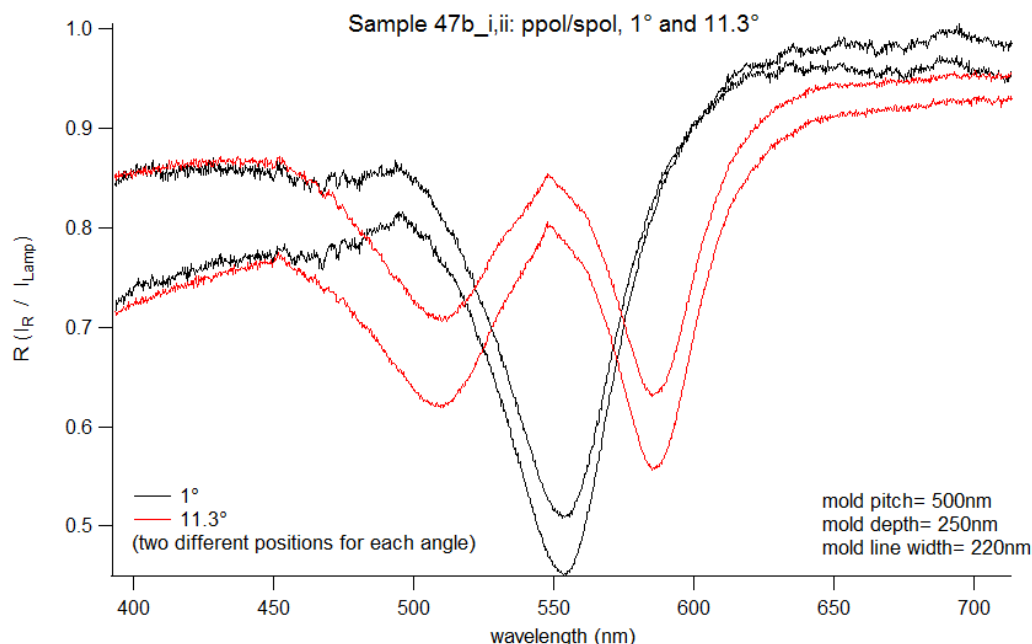


Figure 3.5: Splitting of the grating resonance with angle. The resonance line is shown at the smallest angle (closest to normal incidence) and the largest. Data from only two regions on the grating area are shown here but exhibit reasonable uniformity over the patterned area (other areas were similar in resonance quality). Mold dimensions used to make these grating (via NIL) specifically with a resonance at the desired $\sim 550\text{nm}$ are indicated.

As can be seen, these gratings have a resonance at $\sim 550\text{nm}$ to overlap directly with and enhance the CT-dominated peak around 550nm in PTCDA. This particular sample showed the deepest resonance, about 40%, of all the gratings obtained. Fits to these gratings were carried out as described in the previous section using only the grating part and using a linear background (instead of that of PTCDA). Both Gaussian and Lorentzian line shapes were used and Lorentzians were found to give a slightly better fit. Fit variations also included unconstraining the ΔE from its linear relation with angle and unlinking E_0 between all the angles, allowing it to be different for each angle. Fits were best when ΔE and E_0 allowed more freedom but the fit is more rigorous and trustworthy when restricting these parameters. Restricting them is likewise better for a global fit such as the one used here since linking parameters between each spectrum

(each angle) reduces the number of parameters. Fig. 3.6 shows a fit to the same grating in Fig. 3.5.

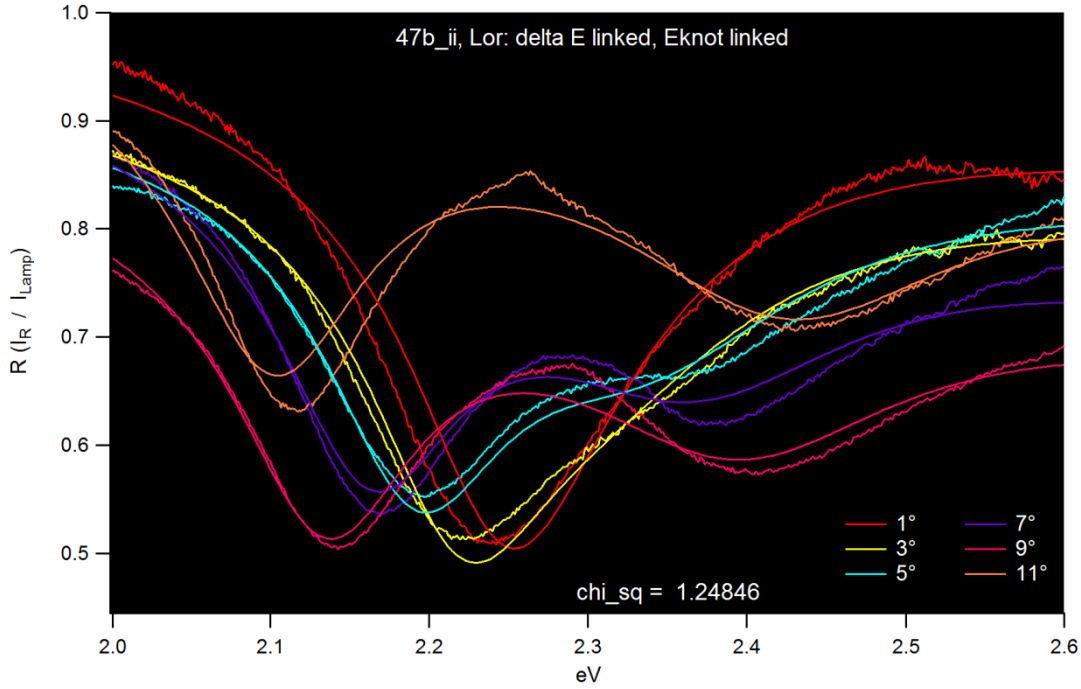


Figure 3.6: A fit to the data shown in Fig. 3.5 for one of the same regions (ii) on the grating as shown in the previous figure. Lorentzian line shapes were used. Parameters are as follows: $E_0 = 2.263\text{eV}$; Slope of $\Delta E = 0.0143\text{eV}$ ($\Delta E = \sim 80\text{nm}$); Area $r = 0.0627$; Area $b = 0.0669$; $\gamma_r = 0.0722$; $\gamma_b = 0.130$. Uncertainties in the parameter values were all less than $\pm 0.4\%$. Only some angles are shown, for clarity in reading the plot.

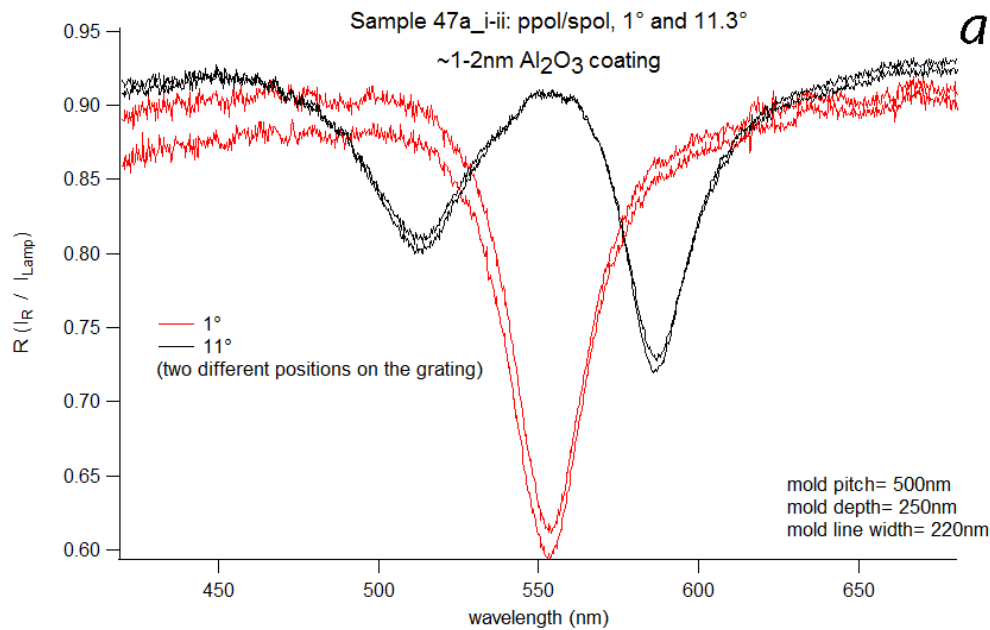
It can be seen in the above figures that the lower wavelength or higher energy, blue-moving resonance peak is systematically wider and shallower than the red-moving peak. This was observed in all gratings and is likely due to the peaks proximity to where silver experiences the onset of interband absorption. Parameters at each angle were used as starting parameters when fitting R spectra taken after oxide deposition on these same gratings in the next section.

Based on these bare grating reflection spectra from multiple sets of gratings, six gratings that showed the most similar optical spectra— resonances in almost the same position, line widths and depths comparable— were chosen to make the coupled plasmon/exciton system. Gratings were grouped by extent of their resonance quality. Three of the gratings exhibited the

best quality resonances, deep and narrow, while the other three showed only good quality – resonances were neither as deep nor as narrow. A total of six gratings were chosen in order to have duplicates in all the experiments described below. In each set of gratings, one was kept bare and PTCDA was deposited directly on top while an aluminum oxide spacer layer was deposited on the other two. The thin 1-2nm of oxide was to act as a dielectric spacer layer to prevent any direct reaction between the organic and the metal while the thick layer was to serve as a control and hopefully attenuate the SP EM field enough to void any plasmonic effect.

3.3.3 Grating with Oxide

As mentioned, four gratings showing reasonable SP resonance features were coated with Al_2O_3 of varying thickness by atomic layer deposition. Thickness of the thicker layer was confirmed with ellipsometry. Fig. 3.7 shows R spectra of one grating that received the thin oxide layer and one that received the thick layer.



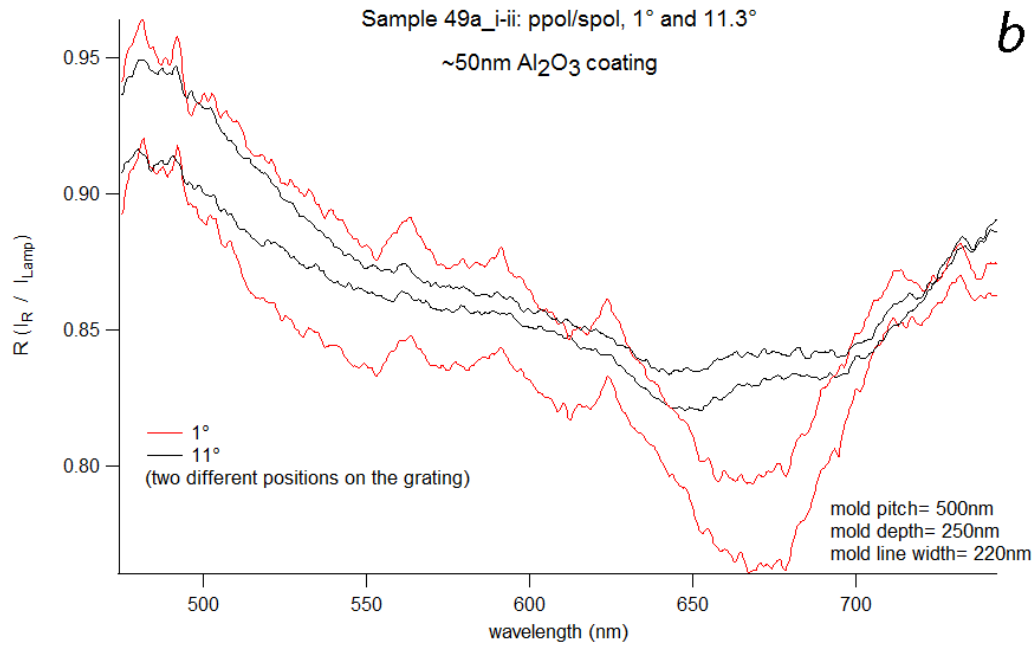


Figure 3.7: R spectra of two gratings post oxide deposition: (a) 1-2nm Al_2O_3 , (b) 50nm Al_2O_3 .

It is immediately evident that normal grating behavior is barely perceptible in the sample with thick oxide. The resonance line shifted, as expected with the addition of a dielectric layer, to about 650nm. This is a shift of 100nm to the red from the original bare grating, 1° incident angle position. The resonance line shows splitting with angle, but the features are entirely too shallow, rendering it impossible to use these gratings as controls. The SP behavior is no longer warranted. On the contrary, the R spectra for the thin oxide layer remain very similar to those of bare grating with no oxide layer. The grating resonance is still at ~550nm. This suggests that, at least with this thickness, the dielectric spacer did not have an effect on the excitation of PTCDA. The two gratings with 1-2nm Al_2O_3 were fit with the same procedure as for the bare grating. An exemplary fit is shown in Fig. 3.8.

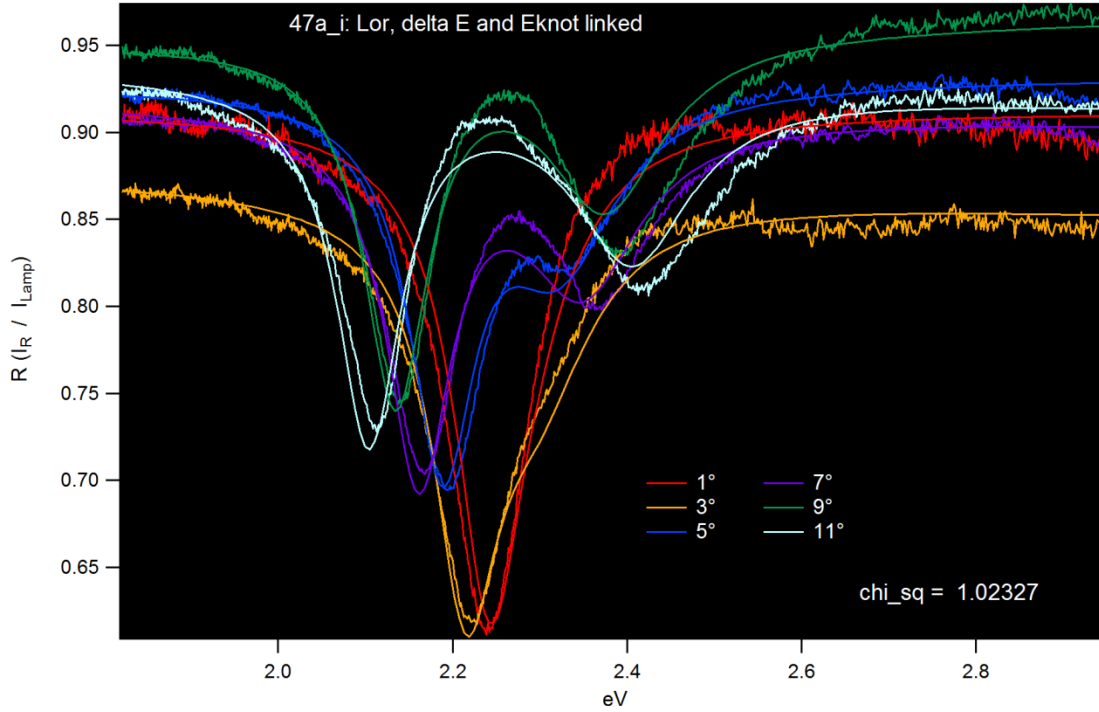


Figure 3.8: Fit to a grating sample from the best resonance quality set with 1-2nm of Al_2O_3 deposited on top. Lorentzian line shapes were used. Parameters are as follows: $E_0 = 2.255\text{eV}$; Slope of $\Delta E = 0.0133\text{ eV}$; Area $r = 0.0291$; Area $b = 0.0249$; $\gamma_r = 0.0451$; $\gamma_b = 0.0811$. Uncertainties in the parameter values were all less than $\pm 0.01\%$. Not all angles shown for visual clarity.

Comparing this fit with that of the other grating with thin oxide, it is evident that the peaks from the splitting resonance line decreased slightly in area and width after oxide deposition, but the grating SP behavior is undoubtedly still present. Parameter values from these fits of grating + thin oxide were used as starting values for fitting R spectra post-PTCDA deposition in the next section.

3.3.4 Grating with Oxide and PTCDA

10nm PTCDA was deposited on all six gratings. The R spectra presented in Figure 3.9 are for two of the samples, with and without the dielectric spacer layer.

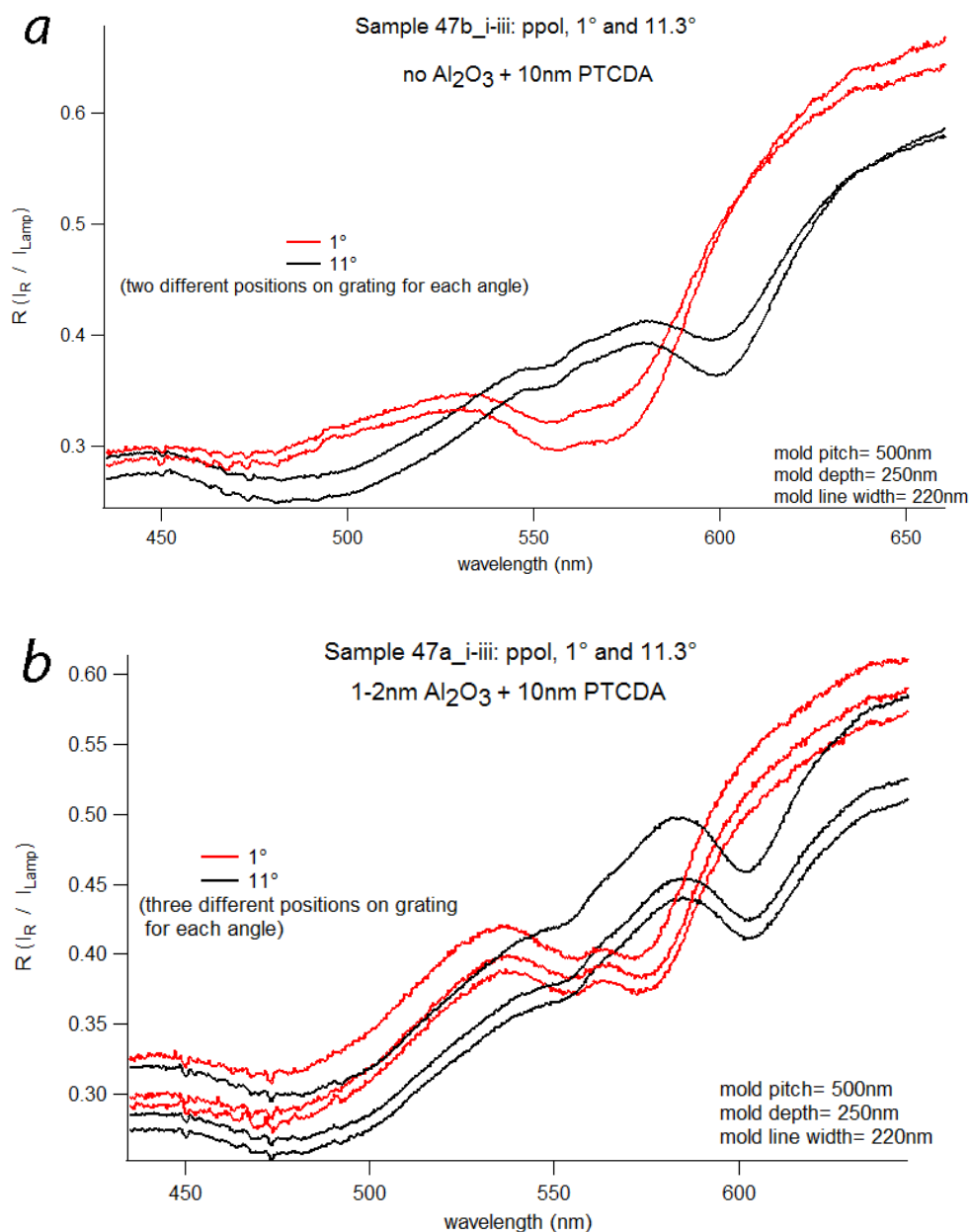


Figure 3.9: (a) Reflectance of 10nm PTCDA on bare grating. (b) Reflectance of 10nm on grating coated with 1-2nm Al₂O₃. At 11°, the red-shifted part of the grating resonance is clearly visible around 600nm for both samples.

Immediately noticeable from the reflectance spectrum of the organic on bare grating is a red shift of ~25nm of the grating resonance from its position at 1° with no coating on top (Fig. 3.5). It does not directly overlap with the 550nm PTCDA excitation. This is due to the Rabi splitting

observed in the simulation as well as to the fact that the grating resonance red shifts with a dielectric coated on top – 10nm PTCDA, in this case. Technically, at 1° , the bump at $\sim 560\text{nm}$ is can no longer be called a CT-dominated state, just as the shifted bump around 575nm no longer corresponds to a pure SPP state. Since the excitations are coupled at zero incidence, and remain so for the first ~ 4 degrees, as the simulation indicates, these peaks are more accurately referred to as some combination of the two excitations. At 11° , only the red-moving part of the grating resonance is clearly visible. Considering a separation of $\sim 80\text{nm}$ between the two peaks at 11° for a bare grating, the blue-moving resonance peak for R spectra of these PTCDA-coated gratings should be around $\sim 530\text{nm}$.

Fits focused on the four samples without the thick oxide and used the full procedure with contributions from both the organic and the grating. They are not finished as of this thesis being written, so no comment can be made on if anticrossing was observed between the SPP and the CT-dominated PTCDA excitation. However, completed fits suggest that the blue SPP dissipates quickly by assigning it very large widths and small amplitudes at higher angles. This is in line with the simulation of Fig. 3.1, which shows only the red SPP. A cause for this may be that as it propagates, the blue SPP reaches energies where PTCDA is heavily absorbing (the mixed CT-FE broadband feature). The absorption dampens its propagation and dissipates the blue SPP.

Whereas on the lower energy side, PTCDA has no significant excitations and the red-shifting SPP experiences a much longer propagation length. In addition, a preliminary study was done with a grating of slightly higher periodicity coated with a thicker, 20nm layer of PTCDA.

Because of the greater periodicity, this grating's resonance was at a higher wavelength, 600nm , and shifted to 650nm with the 20nm PTCDA coating. This kind of sample can also serve as a

control since the resonance is potentially too far red to interact with the CT-dominated PTCDA peak. Fits to the R spectra of this sample did not indicate any plasmon-exciton anticrossing.

3.4 Conclusions

The angle-resolved reflectance measurements of the grating samples at each step in the process of their coating have revealed an expected behavior for the grating resonance. At exactly normal incidence the resonance is at 550nm (confirmed by another measurement setup) and splits as a function of wave vector, resulting in counter propagating SPPs. Although coupling has not yet been observed experimentally, the potential is definitely there as the simulation shows: both the plasmon-exciton anticrossing behavior as well as their Rabi splitting at zero incidence are evidence of coupling. The work also seems to suggest that it is the red SPP, not the higher energy SPP, that seems to couple to the exciton.

Chapter 4

Future Directions for Plasmon-Exciton Coupling in PTCDA

It is evident that the quality of the grating response is crucial. A more intense SP resonance would make extraction of relevant fit data from the fitting procedure more convenient. Improvement of the quality of the resonance would focus on making the SP resonance deeper, $>50\%$, but with maintained narrowness, $\text{FWHM} \leq 50\text{nm}$. This could entail searching via simulation for new grating dimensions that satisfy the shape preference, or possibly altering steps of the current fabrication to achieve lowered variation in the periodicity and line width. Alternative spacer materials or methods for their deposition can be considered to address the issue of the thick spacer layer washing out the grating response. The current state of the research involves finishing fitting of the samples with PTCDA \pm thin oxide. A new set of gratings will allow immediate application of lessons learned from the current set.

Once exciton-plasmon anticrossing is observed with the reflectance measurements, steady-state absorption measurements can be done to verify enhance excited-state absorption. A true control or alteration of coupling between the excited states of the organic semiconductor would be observed as a change in rate of the process as a function of SP coupling. To this end, time-resolved fluorescence experiments can be done on the samples to measure lifetimes of singlet fission and triplet-triplet annihilation.

Similar studies with other absorber materials will contribute to a greater understanding of the behavior of these SP/semiconducting molecular species. Specifically, in the immediate future, a suitable j-aggregate, a well-studied small-molecule organic material, may be deposited on new gratings to prove hybridization in this material system.

Bibliography

- [1] M. Fox. Optical Properties of Solids. 2nd ed. Oxford University Press, 2010.
- [2] S. A. Maier. Plasmonics: Fundamentals and Applications. Springer Science, 2007.
- [3] H. Raether. Surface Plasmons on Smooth and Rough Surfaces and on Gratings. Springer Verlag, 1988.
- [4] A. H. Nicol. Grating Coupled Surface Plasmon Enhanced Fluorescence Spectroscopy. Ph.D. thesis, Johannes Gutenberg-Universität Mainz, 2005.
- [5] A. P. Hibbins. Grating Coupling of Surface Plasmon Polaritons at Visible and Microwave Frequencies. Ph.D. thesis, University of Exeter, 1999.
- [6] I. R. Hooper and J. R. Sambles. Dispersion of surface plasmon polaritons on short-pitch metal gratings. *Phys. Rev. B*, 65(16): 165432, Apr 2002.
- [7] J. White. Surface Plasmon Polaritons. Stanford University.
URL <http://large.stanford.edu/courses/2007/ap272/white1/>
- [8] The 6th International Conference on Surface Plasmon Photonics. Ottawa, Canada. May 2013.
URL <http://www.hospitalite.com/Clients/spp6/index.php?to=12>
- [9] Thorlabs. Products> optical elements> optical mirrors> metallic silver mirrors> graphs.
URL http://www.thorlabs.us/NewGroupPage9.cfm?ObjectGroup_ID=903
- [10] J. A. Dionne, L. A. Sweatlock, H. A. Atwater and A. Polman. Planar metal plasmon waveguides: frequency-dependent dispersion, propagation, localization, and loss beyond the free electron model. *Phys. Rev. B*, 72(7): 075405, Aug 2005.
- [11] R. W. Wood. On a remarkable case of uneven distribution of light in a diffraction grating spectrum. *Proc. Phys. Soc. London*, 18: 269-275, 1902.

- [12] F. J. v. Soest, H. A. G. M. v. Wolferen, H. J. W. M. Hoekstra, R. M. de Ridder, K. Wörhoff and P. V. Lambeck. Laser interference lithography with highly accurate interferometric alignment. *Jap. J App. Phys.*, 44 (9A): 6568-6570, Sept 2005.
- [13] Q. Xie, M. H. Hong, H. L. Tan, G. X. Chen, L. P. Shi and T. C. Chong. Fabrication of nanostructures with laser interference lithography. *J Alloys and Comp.* 449: 261-264, Jan 2008.
- [14] J. d. Boor, N. Geyer, J. V. Wittemann, U. Gösele and V. Schmidt. Sub-100nm silicon nanowires by laser interference lithography and metal-assisted etching. *Nanotech.*, 21: 095302, Jan 2010.
- [15] J. M. Carter, R. C. Fleming, T. A. Savas, M. E. Walsh and T. B. O'Reilly. Interference lithography. Submicron and Nanometer Structures, *MTL Annual Report* 2003.
- [16] Newport. Spatial filters. URL <http://www.newport.com/Spatial-Filters/144910/1033/content.aspx>
- [17] V. Lomakin. Laboratory technique: spatial filtering. University of California, San Diego. URL http://cem01.ucsd.edu/~vitaliy/courses/ece182/182-06_files/SpatialFiltering.pdf
- [18] J. M. Park, W. Leung, K. Constant, S. Chaudhary, T. G. Kim and K. M. Ho. Laser interference lithography for fabricating nanowires and nanoribbons. Chp. 21 in Nanowires – Implementations and Applications. ed. Abbas Hashim. Intech, 2011.
- [19] Y.-L. Yang, C.-C. Hsu, T.-L. Chang, L.-S. Kuo and P.-H. Chen. Study on wetting properties of periodical nanopatterns by a combinative technique of photolithography and laser interference lithography. *App. Surf. Science*, 256: 3683-3687, Jan 2010.
- [20] M. Möbus, N. Karl and T. Kobayashi. Structure of perylene-tetracarboxylic-dianhydride thin films on alkali halide crystal substrates. *J Cryst. Growth*, 116: 495-504, 1992.

- [21] C.I.Pigment Red 224. URL <http://www.chemnet.com/Suppliers/13683/CIPigment-Red-224-1410805.html>
- [22] R. M. Williams. A highly soluble asymmetric perylene- *bis* (dicarboximide)-acceptor system incorporating a methylene bridged methoxybenzene-donor: solvent dependence of charge transfer interactions. *Turk J Chem.*, 33: 727-737, 2009.
- [23] M. Schneider, J. Hagen, D. Haarer and K. Müllen. Novel electroluminescent devices based on perylene-doped Sol-Gel layers. *Ad. Mat.*, 12(5): 351-354, Feb 2000.
- [24] L. Schmidt-Mende, A. Fechtenkötter, K. Müllen, E. Moons, R. H. Friend and J. D. MacKenzie. Self-organized discotic liquid crystals for high-efficiency organic photovoltaics. *Science*, 293: 1119-1122, Aug 2001.
- [25] H. Langhals. Cyclic carboxylic imide structures as structure elements of high stability. Novel developments in perylene dye chemistry. *Heterocycles*, 40(1): 477-500, Jan 1970.
- [26] V. Bulović and S. R. Forrest. Study of localized and extended excitons in 3,4,9,10-perylenetetracarboxylic dianhydride (PTCDA) II. Photocurrent response at low fields. *Chem. Phys.*, 210: 13-25, 1996.
- [27] R. Scholz, I. Vragović, A. Y. Kobitski, M. Schreiber, H. P. Wagner, D. R. T. Zahn. Frenkel exciton model of low temperature photoluminescence in α -PTCDA single crystals. *Phys. Stat. Sol.*, 234(1): 402-410, Sept 2002.
- [28] S. R. Forrest. Ultrathin organic films grown by organic molecular beam deposition and related techniques. *Chem. Rev.*, 97: 1793-1896, Jul 1997.
- [29] M. H. Hennessy, Z. G. Soos, R. A. Pascal Jr. and A. Girlando. Vibronic structure of PTCDA stacks: the exciton-phonon-charge transfer dimer. *Chem. Phys.*, 245: 199-212, Nov 1999.

- [30] G. Mazur and P. Petelenz. *Chem. Phys. Lett.*, 324: 161-165, Apr 2000.
- [31] A. J. Ferguson and T. S. Jones. Photophysics of PTCDA and Me-PTCDI thin films: effects of growth temperature. *J. Phys. Chem. B.*, 110: 6891-6898, Mar 2006.
- [32] A. Palma, A. Pasquarello and R. Car. First-principles electronic structure study of Ti-PTCDA contacts. *Phys. Rev. B*, 65: 155324, Mar 2002.
- [33] B. Krause, A. C. Dürr, K. A. Ritley, F. Schreiber, H. Dosch and D. Smilgies. On the coexistence of different polymorphs in organic epitaxy: α and β phase of PTCDA on Ag(111). *App. Surf. Science*, 175: 332-336, 2001.
- [34] J. Xue, S. R. Forrest. Bipolar doping between a molecular organic donor-acceptor couple. *Phys. Rev. B*, 69: 245322, Jun 2004.
- [35] A. B. Djurišić, C. Y. Kwong, W. L. Guo, Z. T. Liu, H. S. Kwok and W. K. Chan. Spectroscopic ellipsometry of 3,4,9,10-perylenetetracarboxylic dianhydride (PTCDA). *Appl. Phys. A* 77(5): 649-653, 2003.
- [36] M. Knupfer, T. Schwieger, J. Fink, K. Leo and M. Hoffman. Excitons in quasi-one-dimensional organic crystals. *Phys. Rev. B* 66(3): 035208, 2002.
- [37] M. B. Smith and J. Michl. Singlet fission. *Chem. Rev.*, 110(11): 6891-6963, 2010.
- [38] W. Shockley and H. J. Queisser. Detailed balance limit of efficiency of p-n junction solar cells. *J. Appl. Phys.* 32(3): 510-519, 1961.
- [39] M. C. Hanna and A. J. Nozik. Solar conversion efficiency of photovoltaic and photoelectrolysis cells with carrier multiplication absorbers. *J. Appl. Phys.* 100(7): 074510, 2006.

- [40] E. C. Greyson, J. Vura-Weis, J. Michl and M. A. Ratner. Maximizing singlet fission in organic dimers: theoretical investigation of triplet yield in the regime of localized excitation and fast coherent electron transfer. *J. Phys. Chem. B* 114(45):14168-14177, 2010.
- [41] I. Paci, J. C. Johnson, X. Chen, G. Rana, D. Popović, D. E. David, A. J. Nozik, M. A. Ratner and J. Michl. Singlet fission for dye-sensitized solar cells: can a suitable sensitizer be found? *J. Am. Chem. Soc.* 128(51): 16546-16553, 2006.
- [42] S. T. Roberts, R. E. McAnally, J. N. Mastron, D. H. Webber, M. T. Whited, R. L. Brutchey, M. E. Thompson and S. E. Bradforth. Efficient singlet fission discovered in a disordered acene film. *J. Am. Chem. Soc.* 134(14): 6388-6400, Mar 2012.
- [43] S. Singh, W. J. Jones, W. Siebrand, B. P. Stoichef and W. G. Schneider. Laser generation of excitons and fluorescence in anthracene crystals. *J. Chem. Phys.* 42(1): 330-342, 1965.
- [44] N. Geacintov, M. Pope and F. Vogel. Effect of magnetic field on the fluorescence of tetracene crystals: exciton fission. *Phys. Rev. Lett.* 22(12): 593-597, 1969.
- [45] R. E. Merrifield, P. Avakian and R. P. Groff. Fission of singlet excitons into pairs of triplet excitons in tetracene crystals. *Chem. Phys. Lett.* 3(6): 386-388, 1969.
- [46] C. Jundt, G. Klein, B. Sipp, J. Le Moigne, M. Joucla, A. A. Villaeys. Exciton dynamics in pentacene thin films studied by pump-probe spectroscopy. *Chem. Phys. Lett.* 241(1-2): 84-88, Jul 1995.
- [47] R. Österbacka, M. Wohlgenannt, D. Chinn and Z. V. Vardeny. Optical studies of triplet excitations in poly(*p*-phenylene vinylene). *Phys. Rev. B* 60(16): 253-256, 1999.
- [48] G. Lanzani, S. Stagira, G. Cerullo, S. De Silvestri, D. Comoretto, I. Moggio, C. Cuniberti, G. F. Musso and G. Dellepiane. Triplet exciton generation and decay in a red

- polydiacetylene studied by femtosecond spectroscopy. *Chem. Phys. Lett.* 313(3): 525-532, 1999.
- [49] C. Wang, D. E. Schlomadinger, V. Desai and M. J. Tauber. Triplet excitons of carotenoids formed by singlet fission in a membrane. *Chem. Phys. Chem.* 12(16): 2891-2894, 2011.
- [50] C. Wang and M. J. Tauber. High-yield singlet fission in a carotenoid aggregate observed by a picosecond resonance Raman spectroscopy. *J. Am. Chem. Soc.* 132(40): 13988-13991, 2010.
- [51] O. E. Semonin, J. M. Luther, S. Choi, H. Y. Chen, J. Gao, A. J. Nozik and M. C. Beard. Peak external photocurrent quantum efficiency exceeding 100% via MEG in a quantum dot solar cell. *Science* 334(6062): 1530-1533, 2011.
- [52] Y. Takeda, R. Katoh, H. Kobayashi and M. Kotani. Fission and fusion of excitons in perylene crystal studied with VUV and X-ray excitation. *J. Electron Spectrosc. Relat. Phenom.* 78: 423-426, 1996.
- [53] M. Bazilian, I. Onyeji, M. Liebreich, I. MacGill, J. Chase, J. Shah, D. Gielen, D. Arent, D. Landfear and S. Zhengrong. Re-considering the economics of photovoltaic power. *Bloomberg New Energy Finance* May 2010.
- [54] M. Green, K. Emery, Y. Hishikawa, W. Warta and E. D. Dunlop. Solar cell efficiency tables (version 39). *Progress in Photovoltaics: Research and Applications* 20(1): 12-20, 2012.
- [55] B. Kippelen and J. L. Brédas. Organic photovoltaics. *Energy Environ. Science* 2(3): 251-261, 2009.
- [56] H. A. Atwater and A. Polman. Plasmonics for improved photovoltaic devices. *Nat. Mater.* 9: 205-213, Mar 2010.

- [57] E. Engel, K. Leo and M. Hoffman. Ultrafast relaxation and exciton-exciton annihilation in PTCDA thin films at high excitation densities. *Chem. Phys.* 325: 170-177, 2006.
- [58] T. Dienel, A. Krause, R. Alle, R. Forker, K. Meerholz and T. Fritz. Alkali metal doped organic molecules on insulators: charge impact on the optical properties. *Ad. Mat.* 22(36): 4064-4070, 2010.
- [59] M. Hoffmann, K. Schmidt, T. Fritz, T. Hasche, V. M. Agranovich and K. Leo. The lowest energy Frenkel and charge-transfer excitons in quasi-one-dimensional structures: application to MePTCDI and PTCDA crystals. *Chem. Phys.* 258: 73-96, 2000.
- [60] B. Henderson and G. F. Imbusch. Optical Spectroscopy of Inorganic Solids. Oxford UP, 1989.
- [61] M. M. de Souza. Photophysical Studies of Chromophores in Conjugated Polymers and Model Compounds based on Para-phenylenevinylene. Ph. D. thesis. Dept. of Chemistry, Imperial College, 2000.
- [62] M. Pope and C. E. Swenberg. Electronic Processes in Organic Crystals and Polymers. 2nd ed. Oxford UP, 1999.
- [63] M. Friedrich, G. Gavrila, C. Himcinschi, T. U. Kampen, A. Y. Kobitski, H. Méndez, G. Salvan, I. Cerrilló, J. Méndez, N. Nicoara, A. M. Baró and D. R. T. Zahn. Optical properties and molecular orientation in organic thin films. *J. Phys.: Condens. Matter* 15: S2699-S2718, 2003.
- [64] J. Bellessa, C. Symonds, K. Vynck, L. Beaur, A. Brioude and A. Lemaitre. Giant Rabi splitting in metal/semiconductor nanohybrids. *Superlattices and Microstructures* 49: 209-216, 2011.